Solar Radiation Triggers the Bimodal Leaf Phenology of Central African Evergreen Broadleaved Forests

Liyang Liu, Philippe Ciais, Fabienne Maignan, Yuan Zhang, Nicolas Viovy, Marc Peaucelle, Elizabeth Kearsley, Koen Hufkens, Marijn Bauters, Colin Chapman, et al.

AGU ADVANCING EARTH AND SPACE SCIENCES

JAMES | Journal of Advances in Modeling Earth Systems®

RESEARCH ARTICLE
10.1029/2023MS004014

Solar Radiation Triggers the Bimodal Leaf Phenology of Central African Evergreen Broadleaved Forests

Liyang Liu[1,2], Philippe Ciais[2], Fabienne Maignan[2], Yuan Zhang[2], Nicolas Viovy[2], Marc Peaucelle[3], Elizabeth Kearsley[4,5], Koen Hufkens[4,5], Marijn Bauters[4,5], Colin A. Chapman[6,7,8], Zheng Fu[9], Shangrong Lin[10], Haibo Lu[11], Jiashun Ren[1], Xueqin Yang[1], Xianjin He[2], and Xiuzhi Chen[1]

[1]Guangdong Province Key Laboratory for Climate Change and Natural Disaster Studies, School of Atmospheric Sciences, Sun Yat-Sen University & Southern Marine Science and Engineering Guangdong Laboratory (Zhuhai), Zhuhai, China, [2]Laboratoire des Sciences du Climat et de l'Environnement, IPSL, CEA-CNRS-UVSQ, Université Paris-Saclay, Gif Sur Yvette, France, [3]INRAE, Université de Bordeaux, UMR 1391 ISPA, Villenave-d'Ornon, France, [4]BlueGreen Labs, Melsele, Belgium, [5]Department of Environment, Computational and Applied Vegetation Ecology, Ghent University, Ghent, Belgium, [6]Biology Department, Vancouver Island University, Nanaimo, BC, Canada, [7]School of Life Sciences, University of KwaZulu-Natal, Pietermaritzburg, South Africa, [8]Shaanxi Key Laboratory for Animal Conservation, Northwest University, Xi'an, China, [9]Key Laboratory of Ecosystem Network Observation and Modeling, Institute of Geographic Sciences and Natural Resources Research, Chinese Academy of Sciences, Beijing, China, [10]Carbon-Water Research Station in Karst Regions of Northern Guangdong, School of Geography and Planning, Sun Yat-Sen University, Guangzhou, China, [11]Department of Geography, Faculty of Arts and Sciences & Zhuhai Branch of State Key Laboratory of Earth Surface Processes and Resource Ecology, Beijing Normal University, Zhuhai, China

Key Points:

- Solar radiation is an adequate climate factor to drive the bimodal leaf phenology of central tropical African rainforests
- We developed a new phenology scheme with solar radiation-triggered leaf shedding and flushing for the ORCHIDEE land surface model (LSM)
- The ORCHIDEE LSM with the new phenology scheme captures central tropical African rainforests' bimodal leaf phenology and photosynthesis

Supporting Information:

Supporting Information may be found in the online version of this article.

Correspondence to:

X. Chen,
chenxzh73@mail.sysu.edu.cn

Citation:

Liu, L., Ciais, P., Maignan, F., Zhang, Y., Viovy, N., Peaucelle, M., et al. (2024). Solar radiation triggers the bimodal leaf phenology of central African evergreen broadleaved forests. *Journal of Advances in Modeling Earth Systems*, *16*, e2023MS004014. https://doi.org/10.1029/2023MS004014

Received 18 SEP 2023
Accepted 2 JUL 2024

Abstract Central African evergreen broadleaved forests around the equator exhibit a double annual cycle for canopy phenology and carbon uptake seasonality. The underlying drivers of this behavior are poorly understood and the double seasonality is not captured by land surface models (LSM). In this study, we developed a new leaf phenology module into the ORCHIDEE LSM (hereafter ORCHIDEE-AFP), which utilizes short-wave incoming radiation (SWd) as the main driver of leaf shedding and partial rejuvenation of the canopy, to simulate the double seasonality of central African forests. The ORCHIDEE-AFP model has been evaluated by using field data from two forest sites and satellite observations of the enhanced vegetation index (EVI), which is a proxy of young leaf area index (LAI_{Young}) with leafage less than 6 months, as well as six products of GPP or GPP proxies. Results demonstrate that ORCHIDEE-AFP successfully reproduces observed leaf turnover ($R = 0.45$) and young leaf abundance ($R = 0.74$), and greatly improve the representation of the bimodal leaf phenology. The proportion of grid cells with a significant positive correlation between the seasonality of modeled LAI_{Young} and observed EVI increased from 0.2% in the standard model to 27% in the new model. For photosynthesis, the proportions of grid cells with significant positive correlations between modeled and observed seasonality range from 26% to 65% across the six GPP evaluation products. The improved performance of the ORCHIDEE-AFP model in simulating leaf phenology and photosynthesis of central African forests will allow a more accurate assessment of the impacts of climate change in tropical forests.

Plain Language Summary Evergreen broadleaved forests in central Africa near the equator have a unique behavior where their leaf growth and ability to take in carbon peak twice a year. However, the reason underlying this behavior is not well understood, and the current process-oriented terrestrial biosphere models can not represent this double peak. In this study, we integrated a new module, which uses sunlight as the main factor for when leaves fall and new ones grow in the forest, into a popular process-oriented terrestrial biosphere model called ORCHIDEE, to simulate this unique behavior in central African forests (hereafter ORCHIDEE-AFP). We tested our model using real-world data from the forests acquired at the site level and satellite images. The results show that our new model can successfully simulate when leaves change and how much carbon the forests take in. The new model demonstrates better performance than the standard model. Our improved model will be useful for predicting the future of these forests more accurately under climate change.

1. Introduction

Tropical rainforests are of great importance in regulating the global exchange of carbon dioxide, energy, and water between the land surface and the atmosphere (Chen et al., 2021). Despite a perennial canopy, the leaves of

tropical rainforests are periodically shed and rejuvenated, leading to seasonal variations of phenology and carbon uptake (Leff et al., 2012; Sayer et al., 2011; Sun et al., 2022; Yan et al., 2016). The climatic and biotic drivers of tropical leaf phenology are complex, as the seasonality of old leaves dropping and new leaves sprouting varies across different regions (Gong et al., 2022; Wu et al., 2021; Yang et al., 2021).

Africa has the second-largest tropical rainforests in the world (Zhou et al., 2014), representing ∼18% of global tropical forest areas, but has been understudied compared to the Amazonian and Asian tropical rainforests (Guan et al., 2013; Malhi et al., 2013), notwithstanding its important contributions to the global carbon cycle (Adole et al., 2016). While numerous phenological observations have been conducted in tropical Africa, these have predominantly been centered on flowering or fruiting phenology (Abernethy et al., 2018; Adamescu et al., 2018; Babweteera et al., 2018). Extensive and long-term observations of leaf phenology in the tropical African region remain scarce (Abernethy et al., 2018; Couralet et al., 2013; Kearsley et al., 2013, 2024; Lewis et al., 2009). Typically, central tropical African rainforests around the equator (5°N–5°S) have two wet- and two dry-seasons per year (Jiang et al., 2019; Nicholson, 2018; Raghavendra et al., 2018; Sorí et al., 2017; Sun et al., 2022). This unique bimodal phenology (Yan et al., 2016, 2017) differs from that of the Amazonian and Asian tropical forests (de Weirdt et al., 2012; Liu et al., 2021; Xu et al., 2015; Zhang et al., 2016). To complete sparse field observations, satellite sensors have been used to study the leaf phenology of tropical African rainforests (Gond et al., 2013; Guan et al., 2013; Li et al., 2021; Verhegghen et al., 2012). Yet, previous studies did not come up with a unified model but rather analyzed correlations between optical satellite data and climate variables. Water availability was found not to be a dominant limitation of phenology in regions with a marked dry season (Philippon et al., 2016), and radiation availability was found critical in achieving a high level of carbon uptake during the wet seasons (Graham et al., 2003). Furthermore, radiation has been reported to correlate with the bimodal seasonal variations of carbon uptake in tropical African rainforests (Chapman et al., 2018; Li et al., 2021; Yang et al., 2021).

Land surface models (LSMs), such as ORCHIDEE (Krinner et al., 2005), serve as robust tools for studying the global carbon cycle. A precise representation of the leaf phenology and carbon uptake seasonality is mandatory to determine the carbon response to past and future climate change (Caen et al., 2022; Fu et al., 2013; Koven et al., 2011; Peñuelas et al., 2009; Sitch et al., 2003; Wright et al., 2017; Zhou et al., 2021). However, the standard version of ORCHIDEE poorly represents the leaf phenology of tropical rainforests since it lacks appropriate mechanisms that relate phenological signals to climate drivers (de Weirdt et al., 2012; Manoli et al., 2018). Chen et al. (2020, 2021) managed to reproduce the observed canopy phenology of the Amazonian wet rainforests by implementing a climatic-triggering scheme into the ORCHIDEE LSM. This scheme used functions of Vapor Pressure Deficit (VPD) and radiation as prompters of leaf shedding, a process followed by canopy rejuvenation with the allocation of carbon assimilates to leaves. However, it was not adapted to central tropical African rainforests that have a distinct bimodal phenology.

To improve the simulation of central tropical African rainforest leaf phenology, we proposed a new equation using incoming radiation (SWd) as a driver of leaf shedding, adapting the leaf phenology module of Chen et al. (2021) from the Amazon to central tropical African rainforests (hereafter called ORCHIDEE-AFP, African Phenology). The new model was evaluated by using in situ observations from the Yangambi and Kibale sites and seven observation-based gridded products, encompassing a young leaf leaf area index (LAI) proxy, three data-driven GPP products and three remote sensing GPP proxies (Section 2.5.2 and Table S1 in Supporting Information S1). Furthermore, to assess the uncertainty related to climate forcing used in driving the LSM, particularly for SWd, we performed simulations using two different meteorological forcings, with either the CRUJRA (Harris, 2019) or the WFDE5 (Cucchi et al., 2020). The scientific questions addressed in this study are: (a) whether radiation is an adequate climate factor to drive bimodal leaf phenology of central tropical African rainforests, and (b) if so, to what extent can the new phenological scheme contribute to our understanding of photosynthetic investment strategies in central African rainforests.

2. Materials and Methods

2.1. Study Area

As in most LSMs, plant species are grouped into plant functional types (PFTs, Prentice et al., 1992) based on their morphology and behavior. In the ORCHIDEE LSM, vegetation heterogeneity is described using fractions of 15 different PFTs for each grid cell (Boucher et al., 2020). Two PFTs, namely evergreen broadleaved forests and raingreen broadleaved forests, are used to describe tropical forests in the ORCHIDEE LSM. As this study focuses

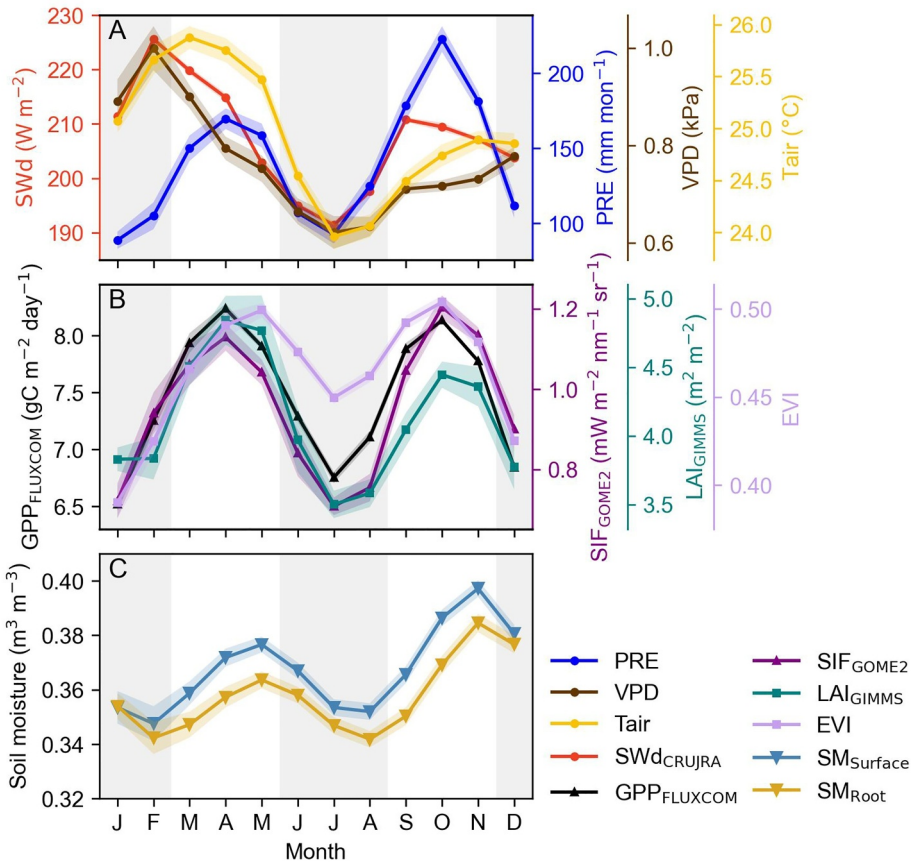

Figure 1. Observed seasonal variations of (a) climate, (b) leaf phenology and photosynthesis, and (c) soil moisture of central tropical African rainforests. The leaf phenology is illustrated by GIMMS LAI (LAI_{GIMMS}) and MODIS EVI, and both FLUXCOM GPP ($GPP_{FLUXCOM}$) and GOME2 SIF (SIF_{GOME2}) are used as photosynthesis representative and proxy, respectively. The SM_{Surf} and SM_{Root} are surface and root-zone soil moisture respectively from the GLEAM v3.7 data set. The light gray vertical backgrounds indicate the dry seasons and the shading areas with color represent the respective standard error of the mean.

on the evergreen broadleaved forests of central tropical Africa, we selected the grid cells with a mean fraction of tropical evergreen broadleaved forests (TroEBF) exceeding 50% from 2000 to 2018 as the study area for regional patterns simulation (Figure S1 in Supporting Information S1). This selection was based on yearly PFT maps derived from the ESA CCI Land Cover maps (Bontemps et al., 2013).

2.2. Seasonality and Modeling Strategy

Across the study area, there are two dry seasons during the periods from December to February (DJF) and July to August (JJA) (Figure 1, gray background), and two wet seasons during the periods from March to May (MAM) and from September to November (SON). For the first half of the year, there are relatively higher SWd, air temperature (Tair) and VPD, along with lower precipitation (PRE) compared to the second half of the year (Figure 1a). This indicates that there is a dryer and brighter season in the first half of the year, while the second half of the year is wetter (lower VPD) and darker (less radiation). Satellite data sets show that both leaf phenology, here illustrated by LAI from the Global Inventory Modeling and Mapping Studies (GIMMS) (Zhu et al., 2013) and enhanced vegetation index (EVI) from the Moderate Resolution Imaging Spectroradiometer (MODIS) (Huete et al., 2002), and carbon uptake by photosynthesis, here illustrated by GPP from FLUXCOM data-driven model (Tramontana et al., 2016) and Solar-Induced chlorophyll Fluorescence (SIF) from the Global Ozone Monitoring Experiment-2 (GOME2, Joiner et al., 2013, 2016), have a double peak seasonal variation. Those two peaks mainly arise in April and October, thus during wet seasons (Figure 1b). The surface (SM_{Surf}) and root-zone (SM_{Root}) soil moisture from the GLEAM v3.7 data set (Martens et al., 2017; Miralles et al., 2011) show a

seasonal variation with two peaks (Figure 1c) generally lagging by about 1 month behind PRE. The value of GLEAM soil moisture in volumetric content, ranging from about 0.34 to 0.4 m^3 m^{-3}, is much larger than that of the wilting point (0.096 m^3 m^{-3}) across the study area (Figure S2 in Supporting Information S1). This suggests that water stress is unlikely to be a trigger of leaf shedding, at least for rainforests around the equator. The small seasonal range of soil moisture variation in GLEAM also suggests that soil moisture is unlikely to be a driver of investment in new leaves, although there may be a specific water potential/soil moisture threshold as a cue to build up new leaves and, conversely, water availability below this threshold as a cue to stop investing into leaf building. In addition, previous studies reported that evaporation is not limited by soil moisture across tropical African rainforests, implying little soil moisture stress in this region during the dry-down period as vegetation may access deep water (Feldman et al., 2018, 2019). Temperature is unlikely a major limiting factor for the litterfall in tropical evergreen forests (De Weirdt et al., 2012; Tang & Dubayah, 2017). Sunlight availability predominantly governs the seasonal leaf phenology across the tropical region (Li et al., 2021). Previous studies proved that VPD is a reliable climate factor triggering leaf shedding of tropical rainforests in the Amazon, while SWd also performs well (Chen et al., 2020, 2021). This is because the seasonal dynamics of VPD and SWd are in phase in the Amazon. This phasing is visible in tropical Africa during the first half of the year (Figure 1a). However, for the second half of the year, this coherence weakens considering the variability of its relative magnitude. Furthermore, the VPD of tropical Africa exhibits little seasonal variation and small amplitude, ranging from 0.6 to 1 kPa (0.6–0.8 kPa for the second half of the year). In contrast, VPD in the Amazon is almost larger than 1 kPa and the maximum VPD goes up to 2 kPa in the wet regions (Green et al., 2020). This suggests that the stability of VPD in tropical Africa may hamper the creation of a reliable signal for leaf shedding, unlike in the Amazon. Additionally, in terms of interannual variability in seasonality, quantified by coefficient of variation (CV, unit: %), SWd (mean CV of 12 months is 0.5%) has little interannual variability compared to Tair (mean CV = 1.2%), SM_{Root} (mean CV = 2.1%), $SM_{Surface}$ (mean CV = 2.0%), VPD (mean CV = 4.1%), and PRE (mean CV = 10.1%) (Figure S3 in Supporting Information S1). Therefore, we proposed that SWd predominantly controls the turnover and flushing of leaves, ultimately driving the double seasonality of leaf phenology and carbon uptake of central tropical African rainforests.

We described the new phenological scheme put into the ORCHIDEE LSM (v6184) (Krinner et al., 2005) for central African rainforests, to become ORCHIDEE-AFP in Section 2.3. Field observed leaf phenology data from two long-term observation sites and seven gridded leaf phenology or photosynthesis data sets were used to evaluate the performance of ORCHIDEE-AFP in simulating leaf phenology (i.e., LAI) and carbon uptake (i.e., GPP) (Section 2.4). The 6-hourly 0.5° CRUJRA v2.0 climate forcing data set, generated by the combination of the Japanese Reanalysis data (JRA) and the Climatic Research Unit (CRU) TS 4.03 data (Harris, 2019; Harris et al., 2014; Kobayashi et al., 2015), was used to drive the model for the period from 2000 to 2018. Previous studies pointed out that central Africa is one of the cloudiest regions across the tropics (Dommo et al., 2018; Wilson & Jetz, 2016), which results in low mean incoming solar radiation (SWd) at the surface, especially during the cool and light deficient dry seasons on the coast of Gabon (Philippon et al., 2019). Considering that SWd is a critical climatic driver of photosynthesis, and to assess the uncertainty related to the climate forcing used to drive the ORCHIDEE LSM, especially regarding the impact of SWd on leaf phenology in our new scheme (Section 2.3), we employed another hourly 0.5° climate forcing data set named WFDE5 (Cucchi et al., 2020) to drive the model. WFDE5 is generated through the application of the WATCH Forcing Data (WFD) methodology to surface meteorological variables derived from the ERA5 reanalysis, with a bias-correction of Tair, SWd and precipitation based on stations CRU and GPCC (Global Precipitation Climatology Centre) observations (Cucchi et al., 2020). Compared with the CRUJRA, SWd from the WFDE5 generally shows a lower solar radiation level, especially during the second half of the year and in the western regions of Gabon and Cameroon (Figure S4 in Supporting Information S1).

2.3. Representing Tropical African Evergreen Canopy Phenology in ORCHIDEE-AFP

In ORCHIDEE-AFP, we implemented a SWd-triggered leaf shedding scheme and leaf flushing scheme, as well as a leaf age-dependent leaf photosynthetic efficiency. A general description of the physical processes related to the energy and water balance, vegetation dynamics and biogeochemical processes in ORCHIDEE can be found in Krinner et al. (2005). Relevant concepts as well as our additions and modifications to the model are presented in the following sections.

2.3.1. Canopy Demography of ORCHIDEE

The ORCHIDEE LSM uses four leaf age classes (class 1 to 4) characterized by their fraction of leaf biomass and mean age, to describe the canopy demography. Leaf age class 1 and leaf age class 4 represent the youngest and the oldest cohorts, respectively. The canopy demography model solves three processes on a daily time step. The first process is the allocation of carbohydrates, in which a fraction of the net primary production (NPP) is allocated to the growth of new leaves (class 1). The second process is the leaf turnover, in which a fraction of the biomass of any leaf class but the last one, turns over to the next age class, and the leaf ages of the four classes are updated accordingly. The third process is leaf shedding starting when a leaf age class reaches an age larger than half the value of the critical leaf age (a_{crit}), at which point leaf loss rapidly increases (with a power law of exponent 4) as the age of the leaf class approaches the critical leaf age (Krinner et al., 2005).

2.3.2. New Leaf Flushing Scheme

In the standard version, ORCHIDEE has a constant carbon allocation coefficient for the leaves (f_{leaf}) of tropical evergreen forests (Krinner et al., 2005). That is, the fraction of NPP allocated to new leaves remains constant until the total LAI exceeds the maximum value (LAI_{max}) which is preset to 6.0 m^2 m^{-2} for tropical evergreen forests according to de Weirdt et al. (2012). In ORCHIDEE-AFP, the carbon allocation toward new leaves (class 1) was parameterized as a function of weekly SWd and LAI of the oldest leaves (class 4), as leaf-flushing of tropical evergreen forests in Africa has been reported to be synchronous with radiation by Guan et al. (2013). Here, we assumed that f_{leaf} is related to the light transmission of old leaves, being an exponentially decreasing function of the LAI of the oldest class ($-0.5*$ LAI_4) (He et al., 2017). The fraction of NPP allocated to new leaves is given by:

$$f_{leaf}^{new} = \min\left[0.99, \left(SWd_{week} \times e^{-0.5LAI_4}/C_1\right)^{C_2} \times f_{leaf}\right] \quad (1)$$

where f_{leaf}^{new} and f_{leaf} are the new and standard allocation fractions of NPP to new leaves (carbohydrates entering age class 1), respectively; SWd_{week} is the running weekly mean short-wave incoming solar radiation (SWd), LAI_4 is the LAI of the oldest leaf age class 4, C_1 and C_2 are empirical coefficients set to 35.0 and 6.0 W m^{-2} in ORCHIDEE-AFP. The constant 0.99 is the ORCHIDEE-specific parameterization to prevent all of the NPP to be used for new leaf construction.

2.3.3. New Leaf Shedding Scheme

The standard ORCHIDEE model (Krinner et al., 2005) assumes no seasonality in leaf phenology for tropical evergreen forests and describes leaf shedding as a function of leaf age:

$$\Delta B_i = B_i \times \min\left\{0.99, \min\left[0.99, \frac{\Delta t}{a_{crit}}\left(\frac{a_i}{a_{crit}}\right)^4\right]\right\} \quad (2)$$

where ΔB_i is the loss of biomass at each time step from age class i, B_i is the leaf biomass of age class i, Δt represents a timestep, a_i is leaf age (unit: days) of class i, a_{crit} is a critical leaf age (unit: days) that is the maximum longevity of a leaf and is set to 730 days for tropical evergreen forests. The constant 0.99 is the ORCHIDEE-specific parameterization to make sure that the turnover rate is never null.

In Equation 2, young leaves hardly have any biomass loss, while older leaves are shed rapidly when they approach the critical leaf age a_{crit}. For leaf age classes 1 to 3, we kept the leaf shedding scheme of Equation 2. But, the leaf-shedding scheme was modified with accelerating the shedding rate of the oldest leaves (class 4) as follows:

$$\Delta B_m = B_m \times \min\left\{0.99, C_3 \times \left[\exp\left(\frac{SWd_{week}}{C_4}\right) - 1.0\right]^{C_5} \times \min\left[0.99, \frac{\Delta t}{a_{crit}}\left(\frac{a_m}{a_{crit}}\right)^4\right]\right\} \quad (3)$$

where SWd_{week} is the running weekly mean SWd (unit: W m^{-2}). C_3, C_4, and C_5 are empirical factors for ORCHIDEE-AFP set to 0.5, 90.0, and 3.0 W m^{-2}, respectively. Figure S5 in Supporting Information S1 shows

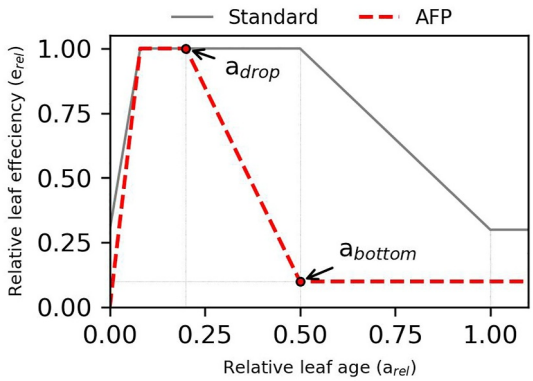

Figure 2. Leaf relative efficiency (e_{rel}) as a function of relative leaf age (a_{rel}). Standard (gray solid line) and AFP (red dashed line) indicate the leaf efficiency formula in the standard version and the new version proposed in this study for central tropical African rainforests, respectively. a_{drop} ($a_{\text{rel}} = 0.2$) and a_{bottom} ($a_{\text{rel}} = 0.5$) indicate the values of a_{rel} when e_{rel} starts to drop down from its maximum ($e_{\text{rel}} = 1$) and when e_{rel} reaches the stable value at 0.1 ($e_{\text{rel}} = 0.1$), respectively.

the impact of SWd on the leaf shedding process, and the sensitivity of leaf shedding to the parameter values. This sensitivity is expressed as the ratio of ΔB_m to B_m ($\frac{\Delta B_m}{B_m}$), computed for different values of C_3, C_4, and C_5.

2.3.4. Adjusted Age-Dependent Leaf Photosynthetic Efficiency

The maximum carboxylation rate of leaves at 25°C ($V_{c,\max 25}$) is scaled by a relative leaf efficiency parameter (e_{rel}, unitless: 0–1) (Ishida and Toma, 1999) which is a function of relative leaf age (a_{rel}, unitless: 0–1). The value of a_{rel} is calculated as the ratio of the leaf age in a cohort to the critical leaf age (a_{crit} = leaf longevity). The leaf critical leaf age (a_{crit}) is never reached due to the formulation of the turnover functions. Younger leaves have a higher photosynthetic capacity than older leaves and the timing of the peak of GPP is thus controlled by the increasing fraction of young leaves (class 1) (Chen et al., 2020; Wu et al., 2016). As both LAI and GPP peak twice a year (Figure 1b), we assumed that, after flushing, a recently emerged leaf reaches its maximum relative efficiency (e_{rel}), defined as the ratio of $V_{c,\max 25}$ divided by its largest value, and maintains this maximum efficiency for a short period. Subsequently, the leaf efficiency decreases, ultimately maintaining a very low value until turnover. Previous studies suggested a minimum e_{rel} range from 0.05 to 0.20 for old leaves in evergreen forests (Misson et al., 2006; Niinemets et al., 2015). Accordingly, in this study, we proposed a new leaf efficiency function for central tropical African rainforests, with four stages, different from the standard version with three stages (Figure 2, gray solid line) (Krinner et al., 2005). For the first stage, from leaf flushing ($a_{\text{rel}} = 0$) to a leaf relative age of 0.08 ($a_{\text{rel}} = 0.08$), the leaf efficiency increases linearly from the minimum ($e_{\text{rel}} = 0$) to the maximum ($e_{\text{rel}} = 1$). In the second stage, it keeps the maximum value ($e_{\text{rel}} = 1$) until $a_{\text{rel}} = 0.2$ (a_{drop}), and during the third stage, it drops down linearly to 0.1 ($e_{\text{rel}} = 0.1$) when relative leaf age reaches 0.5 ($a_{\text{rel}} = 0.5$, a_{bottom}). Finally, during the fourth stage, leaf efficiency stays constant at 0.1 ($e_{\text{rel}} = 0.1$) (Figure 2, red dashed line). In both standard and AFP curve fits, $V_{c,\max 25}$ would reach values close to 0 at age older than 730 days ($a_{\text{rel}} = 1$). In addition, the maximum electron transport capacity at 25°C ($J_{\max 25}$) is also scaled as it is proportional to $V_{c,\max 25}$ (Kattge & Knorr, 2007).

2.4. Simulation Setup

Both versions of the ORCHIDEE model (standard and AFP) were run over a rainforest-dominated domain (7°S–7°N by 3°E−32°E) at a 0.5° spatial resolution. Both 6-hourly CRUJRA climate data and hourly WFDE5 climate data were used to drive the model. Analysis of the daily outputs was performed across the pixels with a fraction of TropEBF >50% (Figure S1 in Supporting Information S1). A spin-up run was performed by cycling on years 1990–1999 for 50 yrs, the model was then run for the 2000–2018 period. It is worth noting that a 1,000-yr spin-up is needed to reach a steady-state equilibrium for carbon reservoirs, but leaf biomass and GPP reach a steady-state much more quickly. Thus, a 50-yr spin-up is sufficient here as this study only focuses on leaf phenology (LAI) and carbon uptake (GPP).

2.5. Model Evaluation

2.5.1. Long-Term In Situ Leaf Phenology Observations

In situ leaf phenology observations are rare in tropical Africa, and acquiring long-term in situ observations is difficult because the countries in this region have low incomes and frequent armed conflicts (Couralet et al., 2013; Malhi et al., 2013). We benefited from long-term leaf phenology observations from two in situ sites, Yangambi (0.77°N, 24.44°E) located in northeastern DR Congo and Kibale National Park (0.45°N, 30.43°E) located in southwestern Uganda (Figure S1 in Supporting Information S1), acquired by the Congolese National Institute for Agronomic Research (INERA) and Ghent University. At the Yangambi site, the weekly leaf turnover incidence (unit: %) of broadleaved evergreen forests, which indicates the fraction of leaves that turned over from younger cohort to older cohort, is available from 1939 to 1953, and we used it to evaluate the seasonal variations of modeled leaf turnover. At the Kibale site, the monthly young leaves abundance (unit: unitless) of broadleaved evergreen forests, which scored from 0 to 4 from no young leaves to young leaves reaching its maximum

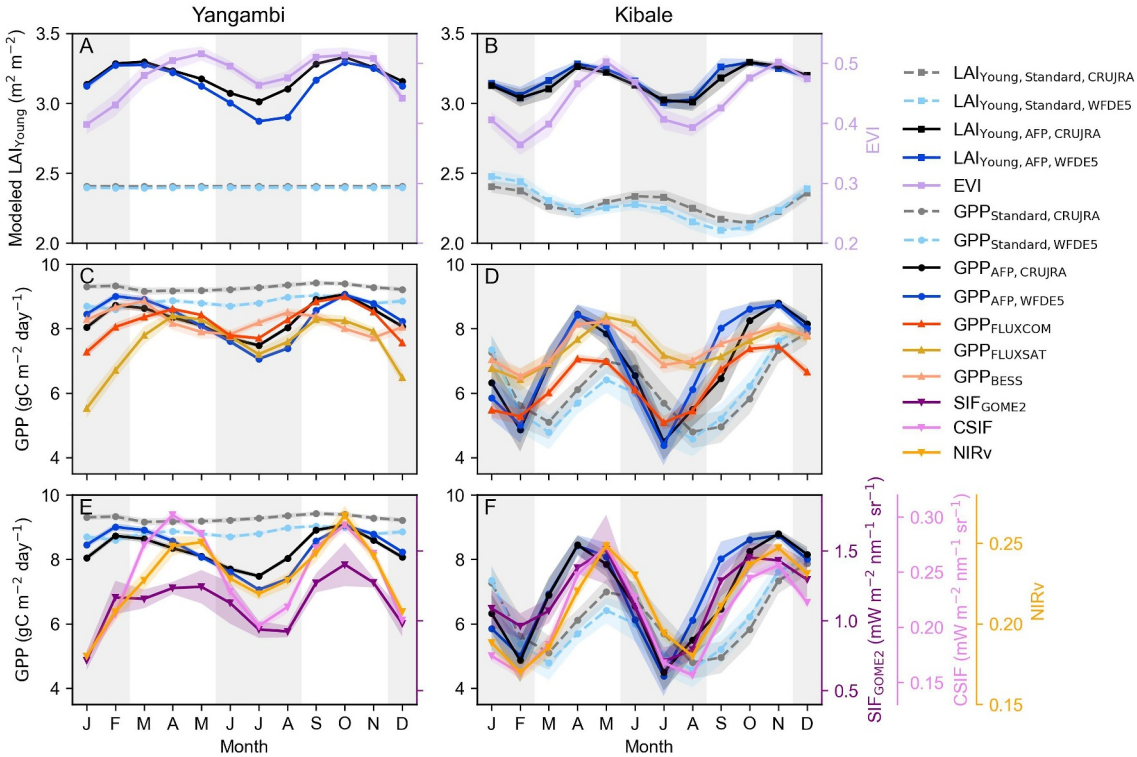

Figure 3. Seasonality of (a–b) young leaf LAI (LAI_{young}) and (c–f) GPP in comparison with observations-based gridded products at two observation sites, (left column) Yangambi, (right column) Kibale. The light gray vertical backgrounds indicate the dry seasons and the shaded areas with color represent the respective standard error of the mean.

proportion in the canopy throughout the year, was provided from June 1998 to December 2013. We used this in situ observation as a proxy for the simulated young leaves LAI (LAI_{young}, class 1). We aggregated all in situ time at a monthly time step.

2.5.2. Gridded Validation Data Sets

All gridded data sets were aggregated at the same spatial and temporal resolutions, which are 0.5° and monthly. For each evaluation product, model outputs were analyzed over the period covered by the data set. Former studies observed that EVI is sensitive to leaf flushing, especially for young leaves aged 2–4 months (Galvão et al., 2011; Gonçalves et al., 2020). Therefore, EVI derived from MODIS (Huete et al., 2002; Xu et al., 2015) were compared with seasonal patterns of simulated young leaves LAI (LAI_{young}), that is the LAI of leaf class 1. Three GPP data-driven products, including FLUXCOM GPP ($GPP_{FLUXCOM}$, Tramontana et al., 2016), FLUXSAT GPP ($GPP_{FLUXSAT}$, Joiner et al., 2018) and BESS GPP (GPP_{BESS}, Jiang & Ryu, 2016a), and three satellite-derived GPP proxies, Solar-Induced chlorophyll Fluorescence (SIF) from Global Ozone Monitoring Experiment-2 (GOME2) ($SIF_{GOME\text{-}2}$, Joiner et al., 2016, 2013), Continuous SIF (CSIF) (Zhang et al., 2018), and the Near-infrared reflectance of terrestrial vegetation (NIRv) from MODIS (Badgley et al., 2017) were used to evaluate the modeled GPP seasonality. More details about all of these seven gridded products are provided in Text S1 and Table S1 of Supporting Information S1.

3. Results

3.1. Model Evaluation at the Site Scale

At both the Yangambi and Kibale sites, the seasonal cycle of MODIS EVI and GPP products/proxies peak twice in the two wet seasons (Figure 3). Notably, the peaks at the Kibale site typically occur with a 1-month lag compared to those at the Yangambi site. Additionally, while the BESS GPP product (GPP_{BESS}) shows bimodal seasonal variation at both sites, it is out of phase when compared with other GPP evaluation products at the

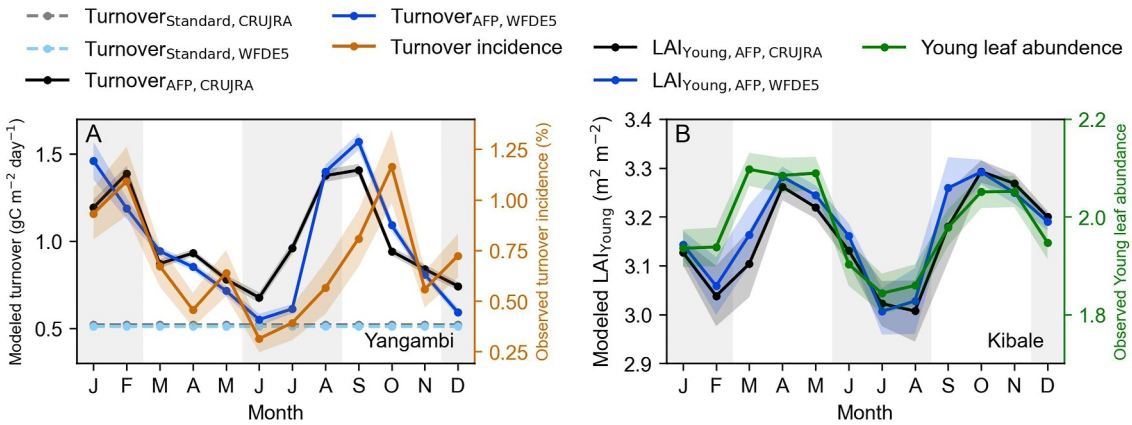

Figure 4. Comparison of simulated variables against in situ observations (a) Modeled leaf turnover (Standard: dashed lines, AFP: solid lines) against in situ observed mean leaf turnover incidence (brown line) at Yangambi, (b) AFP version modeled LAI_{Young} (CRUJRA: black and WFDE5: blue solid lines) against in situ observed mean young leaf abundance (green line) at the Kibale. The light gray vertical backgrounds indicate the dry seasons and the shaded areas with color represent the respective standard error of the mean.

Yangambi site (mean value of Pearson correlation coefficients (R) between GPP_{BESS} and all of the other five GPP products or proxies is -0.19 ± 0.05 (Mean ± Sem)) (Figures 3c and 3e). Regarding the simulation of the seasonal cycle of young leaves LAI (Figures 3a and 3b), the standard model ($LAI_{Young,\ Standard}$, dashed lines) either exhibits a constant value (Figure 3a) or shows an opposite seasonality compared to satellite EVI (Figure 3b). In contrast, the AFP model demonstrates significant improvements, whether driven by the CRUJRA forcing ($LAI_{Young,\ AFP,\ CRUJRA}$, black solid line) or driven by the WFDE5 forcing ($LAI_{Young,\ AFP,\ WFDE5}$, blue solid line). The LAI_{Young} simulated by the AFP model exhibits two peaks, although the first peak is out of phase at both sites, especially at the Yangambi site (Figure 3a). The improvements in the AFP model are also significant in simulating the seasonal variation of GPP. At the Yangambi site (Figures 3c and 3e), the GPP simulated by the standard model ($GPP_{Standard}$, gray line) shows a near-constant value throughout the year. At the Kibale site (Figures 3d and 3f), the $GPP_{Standard}$ (gray dashed line) exhibits a two-peak seasonality but is out of phase compared with evaluation products. In contrast, the GPP simulated by the AFP model demonstrates the two-peak seasonality, aligning more coherently with evaluation products. This occurs whether driven by the CRUJRA forcing ($GPP_{AFP,\ CRUJRA}$, black solid line) or by the WFDE5 forcing ($GPP_{AFP,\ WFDE5}$, blue solid line) (Figures 3c–3f).

We further evaluated the performance of the AFP model by using in situ young leaves/leaf turnover observations (Figure 4). At the Yangambi (Figure 4a), the leaf turnover simulated by the AFP model is in phase with observations (brown line), with a better match to observations when derived from the WFDE5 forcing (blue solid line, $R = 0.57$) compared with that derived from the CRUJRA forcing (dark solid line, $R = 0.45$). At the Kibale (Figure 4b), both simulations with the CRUJRA (dark solid line, $R = 0.74$) and the WFDE5 (blue solid line, $R = 0.79$) produce a young leaf LAI (LAI_{Young}) that matches in situ observed young leaves abundance (green line). This site-scale evaluation gives us confidence in the ability of the SWd-triggered AFP model to simulate the dynamics of leaf phenology in central tropical African rainforests.

3.2. Bimodal Leaf Phenology Across Tropical African Rainforests

At the regional scale, LAI_{Young} of the standard version ($LAI_{Young,\ Standard}$) keeps a constant value of about 2.4 with the CRUJRA forcing and 2.3 with the WFDE5 forcing throughout the whole year (dashed lines in Figure 5a). The AFP-modeled LAI_{Young}, using both the CRUJRA ($LAI_{Young,\ AFP,\ CRUJRA}$) and the WFDE5 forcing ($LAI_{Young,\ AFP,\ WFDE5}$), exhibit a two-peak seasonality. However, the first modeled peak (February to March) precedes that of satellite-derived products (April to May). Additionally, during the second half of the year, the magnitude of LAI_{Young} driven by the CRUJRA forcing ($LAI_{Young,\ AFP,\ CRUJRA}$) is larger than that driven by the WFDE5 forcing ($LAI_{Young,\ AFP,\ WFDE5}$). For the whole study area at the grid cell scale, the Pearson correlation coefficients (R) between AFP-modeled LAI_{Young} with the CRUJRA forcing ($LAI_{Young,\ AFP,\ CRUJRA}$) and satellite-derived products show improvement (Figures 5b and 5d). More than 27% of grid cells have significant positive correlations ($R > 0$ and P-value <0.05) between the modeled seasonal cycle of $LAI_{Young,\ AFP,\ CRUJRA}$ and the seasonal cycle of EVI, computed for a monthly time scale. This is in contrast to the performance of gridded $LAI_{Young,\ Standard}$, which

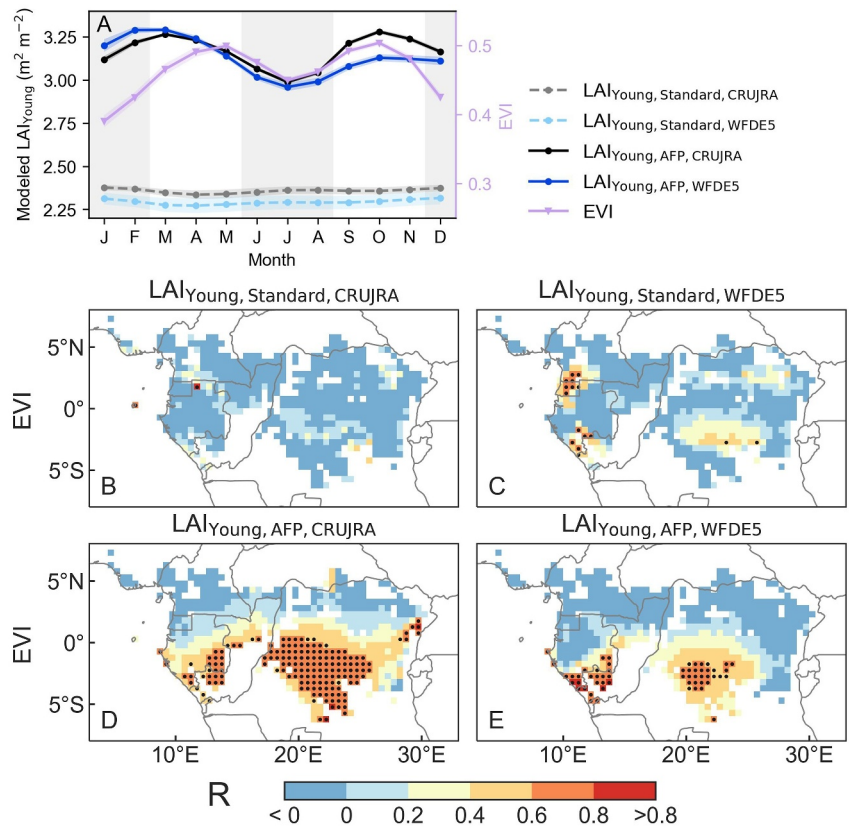

Figure 5. Comparison of modeled young leaf LAI (LAI_{young}) and satellite observations across central tropical African rainforests (a) Seasonality of simulated LAI_{Young} and MODIS EVI. The light gray backgrounds indicate the dry seasons and the shading areas with color represent the respective standard error of the mean (SEM) (b–d) Pearson correlation coefficients (R) between the seasonality of simulated LAI_{young} and seasonality of MODIS EVI. Stippling indicate where the correlation is significant (P-value <0.05).

has hardly any grid cells with a significant positive correlation with EVI (about 0.2% with $R > 0$ and P-value<0.05 for the CRUJRA) (Table S2 in Supporting Information S1). The improvements of gridded $LAI_{Young,\ AFP}$ with the WFDE5 forcing ($LAI_{Young,\ AFP,\ WFDE5}$) are limited and mainly show a positive correlation with EVI over the southern region (Figures 5c and 5e). Particularly, only about 9% of grid cells show a significant positive correlation between $LAI_{Young,\ AFP,\ WFDE5}$ and EVI, although the proportion of positive correlation has increased from about 38% for the standard model to about 47% for the AFP model. In general, gridded $LAI_{Young,\ AFP}$ with the CRUJRA forcing (median value of R at the grid cell scale (R_{Median}) is 0.31) performs better in comparison with EVI than that of the WFDE5 forcing ($R_{Median} = -0.04$) for the whole study area (Table S2 in Supporting Information S1). This difference is attributed to the parameter calibration of the new model, which depends on the CRUJRA forcing data. It is worth noticing that the performance of the AFP model increases from north to south, quantified by the correlation coefficient between AFP modeled LAI_{Young} and EVI (Figures 5d and 5e). The synchronicity between PRE and SWd also increases from north to south (Figure S6 in Supporting Information S1). This suggests that the proposed SWd-triggered phenology scheme is more robust in modeling leaf phenology in regions where PRE and SWd are synchronous.

3.3. GPP Seasonality

The seasonality of modeled GPPs from the standard and AFP versions using the CRUJRA and WFDE5 climate forcing data are compared with different evaluation products in Figure 6. In general, AFP-modeled GPPs (GPP_{AFP}) with both the CRUJRA ($GPP_{AFP,\ CRUJRA}$, black line) and WFDE5 ($GPP_{AFP,\ WFDE5}$, blue line) forcings exhibit a two-peak seasonality, especially for $GPP_{AFP,\ CRUJRA}$. Modeled GPP increases from the beginning of the year and peaks in March, then drops until reaching a minimum in July, and after that, increases again and reaches

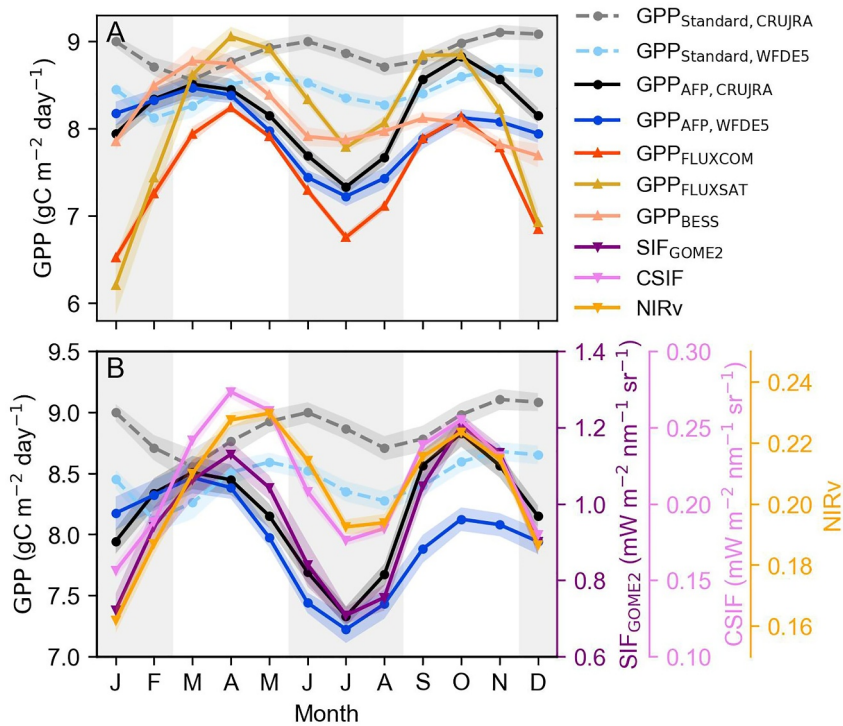

Figure 6. Seasonality of simulated GPP in comparison with GPP/GPP proxies across the central tropical African rainforests. The light gray vertical backgrounds indicate the dry seasons and the shaded areas with color represent the respective standard error of the mean.

its second peak in October. This is generally consistent with most GPP evaluation products, except for GPP_{BESS}, for which the second peak is much smaller than the first one (salmon line in Figure 6a) and seasonal variation shows poor consistency with that of the other products (Figure S6 in Supporting Information S1). Across the central tropical African rainforests, most GPP products and proxies usually reach their first peak during the period from February to March (Figure S8 in Supporting Information S1), and the second peak during the period from September to October (Figure S9 in Supporting Information S1). In comparison, simulated GPP_{AFP}, driven by both the CRUJRA forcing ($GPP_{AFP, CRUJRA}$) and WFDE5 forcing ($GPP_{AFP, WFDE5}$), usually reach a first peak during the period from January to February, preceding evaluation products by about 1 month (Figure 6, Figure S8 in Supporting Information S1).

Considering the spatiotemporal heterogeneity of water supply and light availability in the study area, we split it into four sub-regions (Figure 7a and Figure S10 in Supporting Information S1) using a K-means clustering analysis (Text S2 in Supporting Information S1) based on the seasonality of precipitation (PRE) and SWd data from the CRUJRA forcing. Interestingly, a clustering based on GPP_{AFP} derived from the CRUJRA forcing would show the same patterns as the classification based on PRE and SWd (Figure S10b in Supporting Information S1). In general, GPP products in the four regions show a two-peak seasonality at the regional scale but have different amplitudes. The western regions in Gabon and Cameroon (NW and SW, Figures 7b and 7f) have a relatively lower observed GPP than eastern regions (NE and SE, Figures 7d and 7h), especially for the SW region (Figure 7d). This is because western regions are much darker (Figure S4 in Supporting Information S1) and the significantly lower light availability (Figure 7d) hampers photosynthesis throughout the year (Philippon et al., 2019). The correlations between GPP_{AFP} with the CRUJRA forcing and GPP of the evaluation products of the four sub-regions (Table S3 in Supporting Information S1) show that GPP_{AFP} performs well in the southern sub-regions (SW: $R = 0.61 \pm 0.086$ (Mean $\pm$ Sem), SE: $R = 0.75 \pm 0.089$). However, its performance is less satisfactory in the NE ($R = 0.53 \pm 0.089$) and NW ($R = 0.34 \pm 0.091$) sub-regions, especially during the period from January to March in the NE (Figure 7c). During this period, the observations show lower photosynthetic capacity which may have arisen from insufficient water supply due to low precipitation or large water demand attributed to high VPD, despite favorable light conditions, while the AFP-modeled GPP maintains a relatively

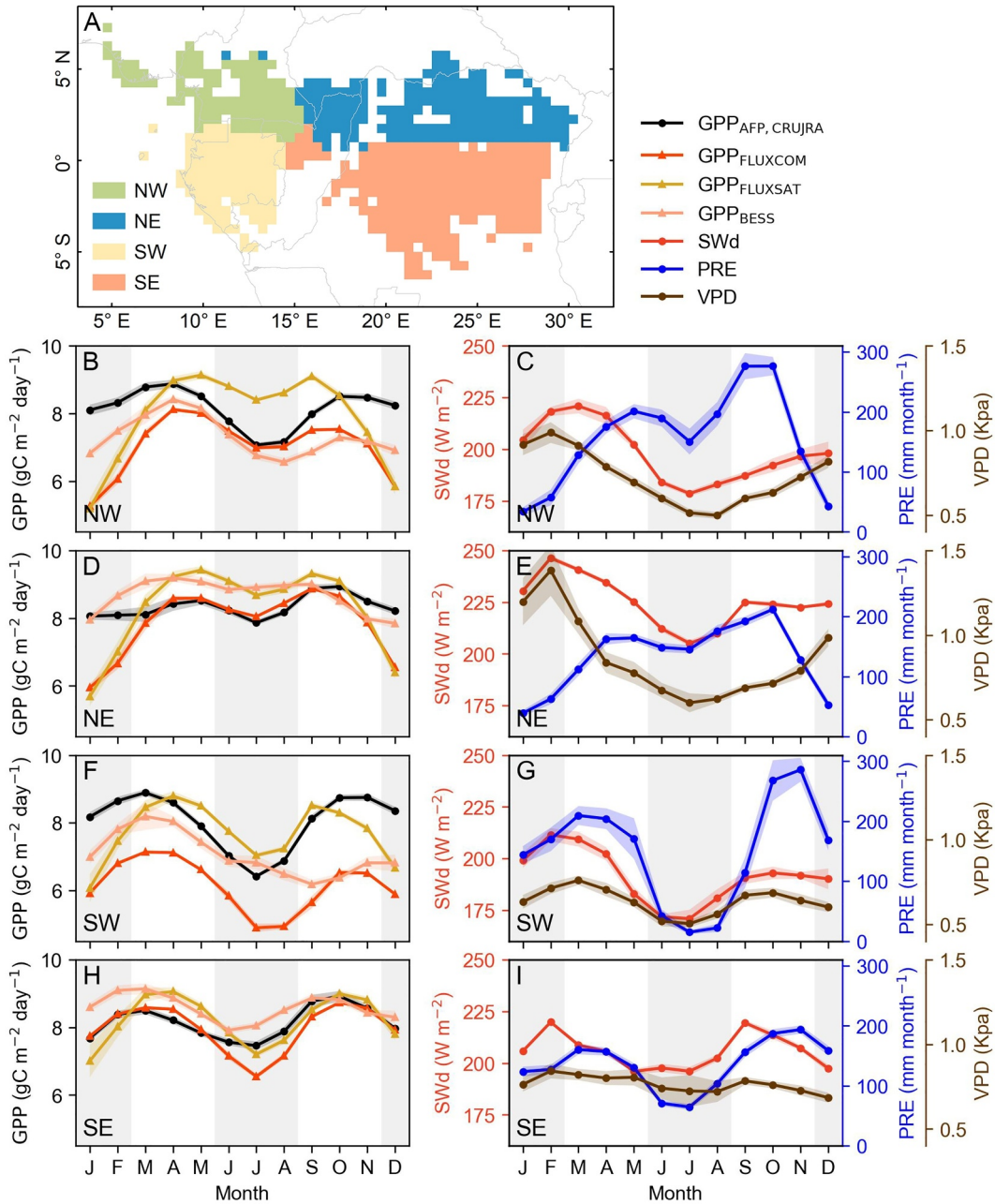

Figure 7. Comparison of simulated GPP_{AFP} with the CRUJRA forcing ($GPP_{AFP, CRUJRA}$) and GPP products for 4 sub-regions classified by the K-means clustering analysis. The 4 sub-regions are the northwestern region (NW), northeastern region (NE), southwestern region (SW), and southeastern region (SE). The light gray vertical backgrounds indicate the dry seasons and the shaded areas with color represent the respective standard error of the mean (SEM). The same comparison but for 3 GPP proxies is shown in Figure S12 of Supporting Information S1.

higher value during this period. Furthermore, the seasonal variation of VPD show divergent partten between south (SW and SE) and north (NW and NE) regions. Particularly in the southeastern region (SE) where the seasonal variation of VPD is minimal and exhibits a near-linear decreasing trend (Figure 7i). Another simulation that uses the VPD-triggered leaf-shedding scheme proposed by Chen et al. (2021) (Figure S11 in Supporting Information S1) shows an unimodal seasonal cycle and fails to capture the second peak. This supports the assumption that SWd is a more reliable leaf-shedding trigger than VPD in tropical African rainforests.

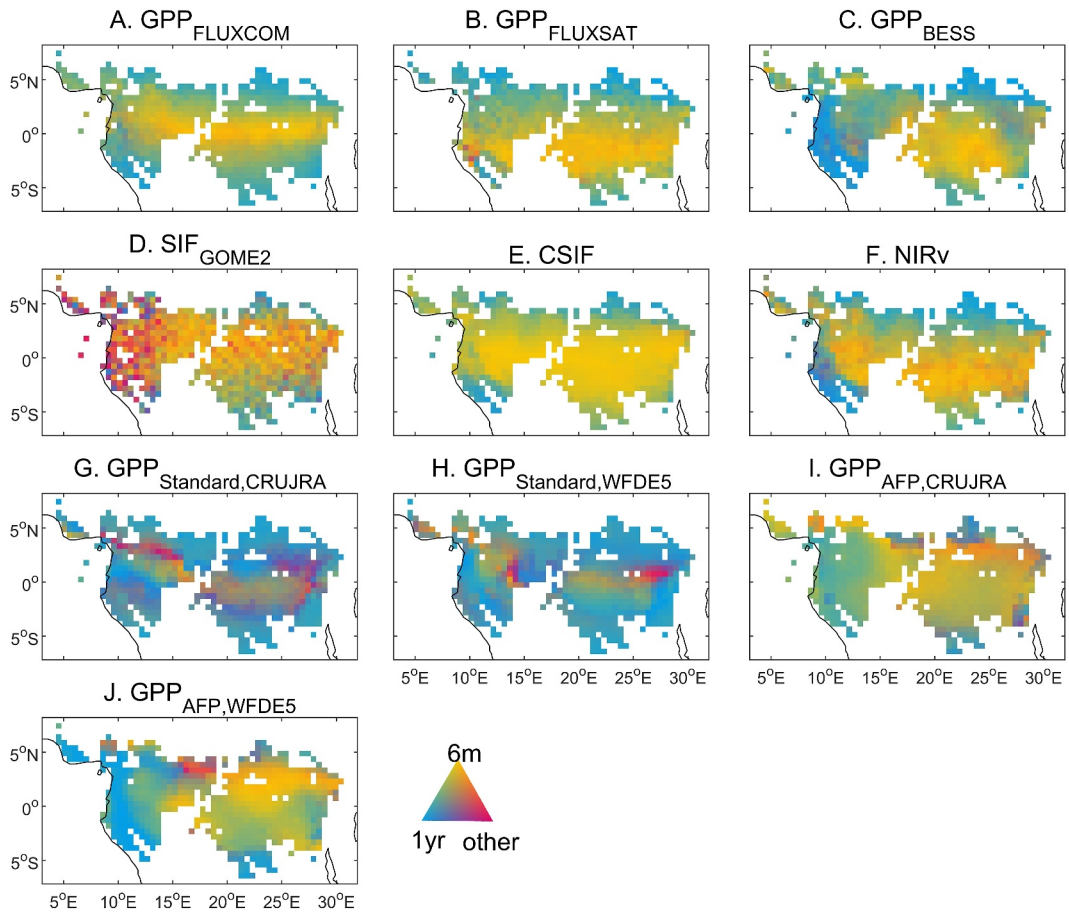

Figure 8. Period of the seasonal cycle of GPP and GPP proxies of central tropical African rainforests. The period is detected using a power spectral analysis (Bradley et al., 2011). The golden grid cells indicate a two-peak (6-monthly) seasonality. The classification of "other" represents the seasonal cycle of grid cells less than 6 months (6 m) or more than 1 yr (1 yr).

The power spectrum analysis (Bradley et al., 2011) is applied to GPP products and proxies (Figures 8a–8f) to identify their dominant periodicity modes of the seasonal variability. The results show that a large fraction of grid cells have a two-peak seasonality across the central tropical African rainforests (golden grid cells in Figure 8), especially along the equator. The GPPs simulated by the standard version ($GPP_{Standard}$, Figures 8g and 8h) could hardly reproduce this two-peak seasonality. In general, GPPs simulated by the AFP version (GPP_{AFP}) better represent the spatial extent of the areas with a two-peak seasonality (Figures 8i and 8j), even though they remain relatively poor in the ever-wet western coastal region when compared with most of the evaluation products (this region is affected by extreme high cloudiness and remote sensing estimates are also more uncertain). The GPP_{AFP} based on the WFDE5 forcing ($GPP_{AFP,\ WFDE5}$, Figure 8j) exhibits the degraded two-peak seasonality from north to south around the latitudes between 15°E and 30°E.

The Pearson correlation coefficients (R) between the seasonal variation of modeled GPP and that of evaluation products at the grid cell level are shown in Figure 9. For the simulated GPP derived from the CRUJRA forcing, compared with the three GPP products (Figures 9a, 9c, 9m and 9o, Figures S13a, S13c, S13g and S13i in Supporting Information S1), the positive correlations between GPP_{AFP} ($GPP_{AFP,\ CRUJRA}$) and $GPP_{FLUXCOM}$ (R_{Median} = 0.67), $GPP_{FLUXSAT}$ (R_{Median} = 0.47), GPP_{BESS} (R_{Median} = 0.56) are much larger than that of $GPP_{Standard,\ CRUJRA}$ (R_{Median} are 0.39, 0.12 and 0.29 for $GPP_{FLUXCOM}$, $GPP_{FLUXSAT}$ and GPP_{BESS} respectively). Especially, the proportions of grid cells showing a significant positive correlation ($R > 0$ and P-value <0.05) are increased from about 27%, 10% and 18% in the standard version to about 65%, 30% and 48% for $GPP_{FLUXCOM}$, $GPP_{FLUXSAT}$ and GPP_{BESS}, respectively (Table S4 in Supporting Information S1). We also find the improvements when comparing $GPP_{AFP,\ CRUJRA}$ with satellite-derived GPP proxies (Figures 9d, 9f, 9p and 9r, Figures S14a, S14c, S14g and S14i in Supporting Information S1). The correlations between GPP_{AFP} with the CRUJRA forcing

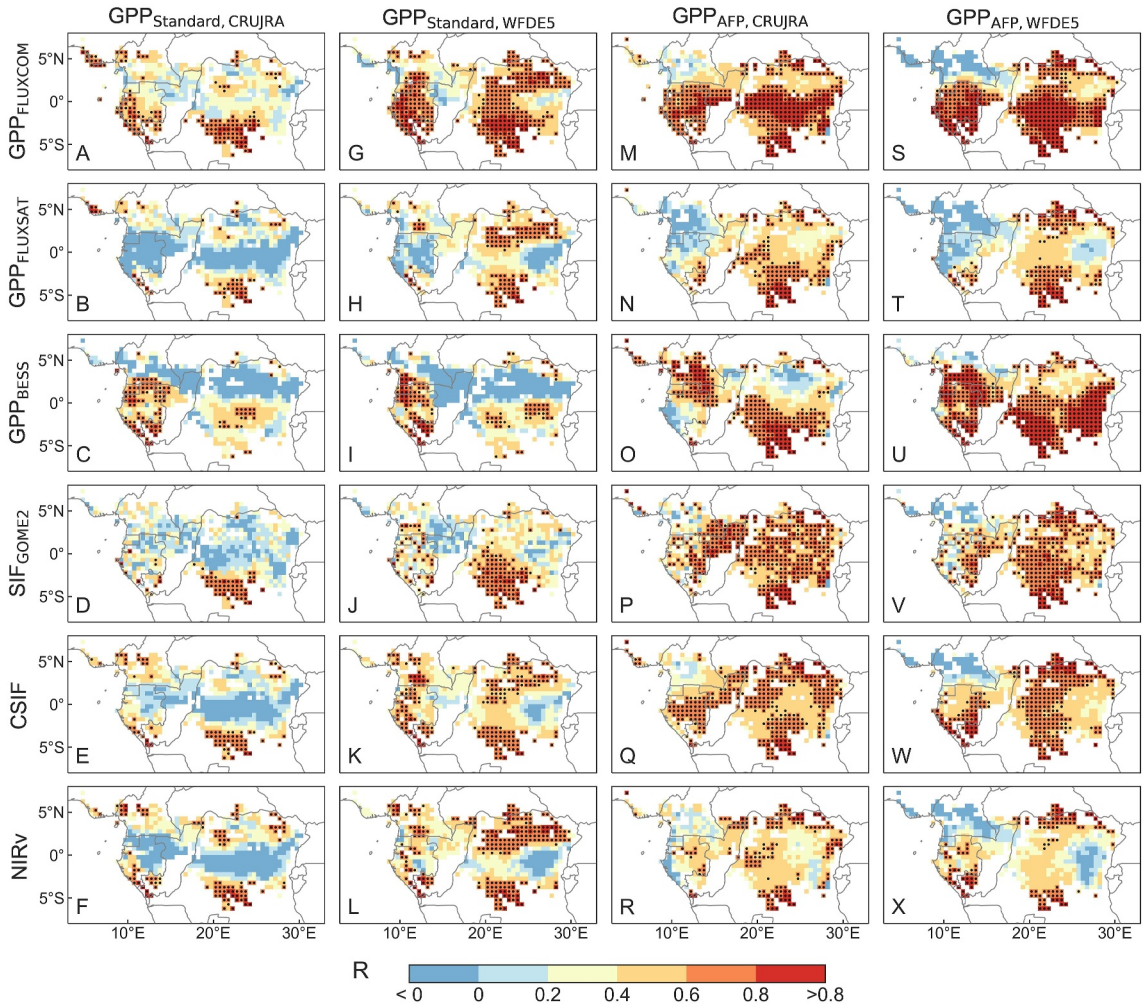

Figure 9. Maps of Pearson correlation coefficients (R) between the seasonal cycles of simulated GPP and GPP evaluation products and proxies. The first two columns are for $GPP_{Standard}$ with the CRUJRA forcing ($GPP_{Standard,\ CRUJRA}$) and the WFDE5 forcing ($GPP_{Standard,\ WFDE5}$) respectively, the third and fourth columns are for GPP_{AFP} with the CRUJRA forcing ($GPP_{AFP,\ CRUJRA}$) and the WFDE5 forcing ($GPP_{AFP,\ WFDE5}$) respectively. The first to the last row represent $GPP_{FLUXCOM}$, $GPP_{FLUXSAT}$, GPP_{BESS}, SIF_{GOME2}, CSIF and NIRv, respectively. Stippling indicate where the correlation is significant (P-value <0.05).

and SIF_{GOME2} (R_{Median} = 0.65) and CSIF (R_{Median} = 0.60) have more than doubled when compared with that of $GPP_{Standard,\ CRUJRA}$. About 65% and 57% of the grid cells of $GPP_{AFP,\ CRUJRA}$ are significantly positively correlated with SIF_{GOME2} and CSIF respectively. It is greatly improved compared with $GPP_{Standard,\ CRUJRA}$ (about 11% and 14% for SIF_{GOME2} and CSIF, respectively) (Table S4 in Supporting Information S1). The $GPP_{AFP,\ CRUJRA}$ shows a better correlation with NIRv (R_{Median} = 0.47, about 26% of grid cells with $R > 0$ and P-value<0.05) than that of $GPP_{Standard,\ CRUJRA}$ (R_{Median} = 0.26, about 18% of grid cells with $R > 0$ and P-value<0.05), but the improvement is limited when compared with that estimated with SIF_{GOME2} and CSIF (Table S4 in Supporting Information S1).

The AFP-modeled GPP using the WFDE5 forcing exhibits similar improvements to those using the CRUJRA forcing when compared to most of the evaluation products (Figures 9g, 9l, 9m and 9r). The improvement of AFP model derived from the WFDE5 forcing ($GPP_{AFP,\ WFDE5}$) is the most significant when using GPP_{BESS} as reference data (Figures 9i and 9u), in which the proportion of grid cells showing a significant positive correlation and the R_{Median} are increased from about 21% to 0.3 to about 71% and 0.72%, respectively (Table S4 in Supporting Information S1). This is followed by improvements when using $GPP_{FLUXCOM}$ (Figures 9g and 9s) and $GPP_{FLUXSAT}$ (Figures 9h and 9t) as reference data. When comparing modeled GPP derived from WFDE5 forcing with satellite-derived GPP proxies, the R_{median} estimated from SIF_{GOME2} (Figures 9j and 9v) and CSIF (Figures 9k and 9w) are increased from 0.39 to 0.49 for standard model ($GPP_{Standard,\ WFDE5}$) to 0.6 and 0.57 for

AFP model (Table S4 in Supporting Information S1), respectively. However, the AFP model ($GPP_{AFP,\ WFDE5}$) shows a poorer performance than the standard model ($GPP_{Standard,\ WFDE5}$) when compared with NIRv (Figures 9l and 9x), with the proportion of grid cells showing a significant positive correlation and R_{Median} decreasing from 39% to 0.48%–21% and 0.39%, respectively (Table S4 in Supporting Information S1). In general, the improvement of the AFP model in simulating GPP is mainly in the southern region, which is attributed to the improved performance in capturing leaf phenology of the AFP model (Figure 5).

Several products are employed to evaluate the performance of the AFP model in simulating GPP seasonality, there are some differences among those products in spatial and temporal patterns, as well as in amplitude (Figures 6–9). GPP from the BESS product shows a significantly different seasonal variation compared to other products (Figures 6 and 8) related to a previously identified limitation for tropical evergreen forests (Jiang & Ryu, 2016a). This discrepancy is likely attributed to the saturation effects of optical remote sensing. Total LAI, an important input parameter in the BESS product algorithm (Ryu et al., 2011), relies on optical remote sensing (MODIS LAI), which tends to saturate in dense canopies (Liu et al., 2022; Zeng et al., 2023), especially over tropical rainforests where the total LAI usually shows little seasonal variability throughout the year (Wu et al., 2016). This also explains why direct validation of model-simulated total LAI with satellite LAI products is unreliable. For the GPP proxies (i.e., NIRv and SIF), from a mechanistic perspective, the NIRv describes the relationship between canopy light capture and GPP (Badgley et al., 2017), while SIF characterizes productivity by measuring light emitted by chlorophyll (Joiner et al., 2016). Compared with the CSIF (Figure 8d), the results of the power spectrum analysis of SIF_{GOME} are noisier (Figure 8e), and the distribution of grid cells showing a significant positive correlation ($R > 0$ and P-value<0.05) between AFP modeled GPP and observed SIF is more dispersed (Figures 9q and 9w). This may be attributed to the uncertainty of the SIF_{GOME2} due to sensor degradation in GOME2 (Zhang et al., 2018). While there are some differences among GPP evaluation products, they display the robustness of the double peak seasonality of tropical African rainforests. In addition, it is worth noting that modeled GPPs with the CRUJRA forcing always have a better correlation with $GPP_{FLUXCOM}$ than that with other GPP products (Figure 9, Table S4 in Supporting Information S1); it is likely because $GPP_{FLUXCOM}$ is extrapolated using CRUJRA meteorological fields (Jung et al., 2020).

4. Discussion

The variation of GPP is influenced by the variations in leaf-age-dependent $V_{c,\ max}$, which reveal the photosynthetic investment strategy of forests. To better understand this strategy in central African rainforests with our new phenology scheme, we tested the impact of different threshold values of the relative leaf age (a_{rel}) when e_{rel} starts to drop down from its maximum value ($e_{rel} = 1$) (hereafter a_{drop}), and when e_{rel} reaches its minimum stable value at 0.1 ($e_{rel} = 0.1$) (hereafter a_{bottom}) on GPP. We tested two values of a_{drop} (0.2 and 0.3) and three values of a_{bottom} (0.4, 0.5 and 0.6). Figure 10 displays four of those six combinations of a_{drop} and a_{bottom}. The results show that the GPP seasonal cycle simulated with those four pairs of a_{drop} and a_{bottom} reproduce a double peak, while its mean value and amplitude are sensitive to the assumed seasonal variations in leaf-age-dependent $V_{c,\ max25}$ related to a_{drop} and a_{bottom}. When a_{drop} increases from 0.2 to 0.3 (dark and purple curves), the amplitude of the modeled GPP cycle decreases from 1.50 to 0.75 gC m^2 day^{-1}, and mean GPP increases from 8.18 to 8.96 gC m^2 day^{-1}. As a_{bottom} increased (blue, dark and cyan curves), the amplitude of the GPP seasonal cycle first increased from 1.28 gC m^2 day^{-1} ($a_{bottom} = 0.4$) to 1.50 gC m^2 day^{-1} ($a_{bottom} = 0.5$), and then drops down to 0.96 gC m^2 day^{-1} ($a_{bottom} = 0.6$). The corresponding mean GPP are 7.92, 8.18 and 9.40 gC m^2 day^{-1}, respectively (Table S5 in Supporting Information S1). The above-mentioned tests with different parameterizations of a_{drop} and a_{bottom} show that the empirical values ($a_{drop} = 0.2$, $a_{bottom} = 0.5$) are likely the optimal choice for simulating the GPP seasonality of tropical African rainforests, although other values also produce a double peak seasonality.

The leaf longevity of tropical forests varies widely, ranging from about 6 months to over 2 yrs, depending on the species (Menezes et al., 2022; Santiago & Wright, 2007). Notably, approximately 2.2% of species comprise 50% of tropical trees in tropical Africa (Cooper et al., 2024). Tropical African trees may have short leaf longevity due to a higher levels of herbivory (Coley & Barone, 1996; Winbourne & McCulloch, 2022), as a result of their high foliar Nitrogen content (Vallicrosa et al., 2021). Indeed, according to the leaf economic spectrum (Osnas et al., 2013; Shipley et al., 2006; Wright et al., 2004), there is a trade-off between leaf longevity (a_{crit}) and maximum photosynthetic capacity (A_m) in different species, a relationship that can be expressed by equating A_m to a_{crit} raised to the power of α (α is a constant) (Osnas et al., 2013; Wright et al., 2004). A_m can be further interpreted as the integral of relative leaf efficiency ($A_{integral}$), and according to Figure 2, this integral ($A_{integral}$) can be further

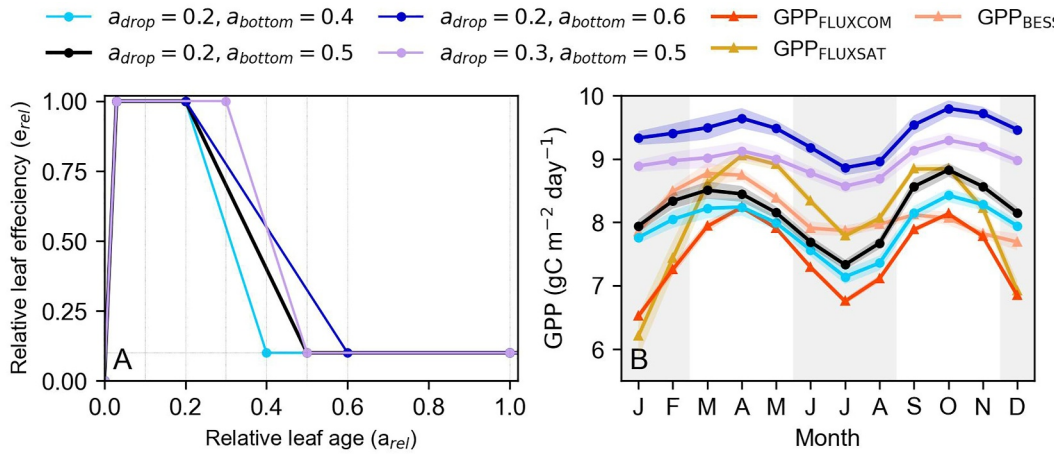

Figure 10. GPP seasonality for different a_{drop} (blue, dark and cyan: 0.2, purple: 0.3) when e_{rel} starts to drop down from maximum value, and for different a_{bottom} (blue: 0.4, dark and purple: 0.5, cyan: $a_{\text{bottom}} = 0.6$) when e_{rel} reaches the stable value at 0.1 (a) e_{rel} as a function of a_{rel}, (b) Simulated GPP seasonality of the whole study area. The light gray vertical backgrounds indicate the dry seasons and the shaded areas with color represent the respective standard error of the mean.

simplified by our formula with a_{drop} and a_{bottom} (Equation 4). Therefore, the triad of parameters a_{crit}, a_{drop} and a_{bottom} can be viewed as representing a typical "group of species" (Equations 4 and 5).

$$A_{\text{integral}} = [a_{\text{drop}} + (a_{\text{bottom}} - a_{\text{drop}}) \times 0.5 + (1 - a_{\text{bottom}}) * 0.1] \tag{4}$$

$$A_{\text{integral}} = {a_{\text{crit}}}^{\alpha} \tag{5}$$

where A_{integral} is the integral computed from the relative leaf efficiency, equivalent to a mean value of $V_{c,\max 25}$ over the leaf age, α is a constant, a_{drop} is the threshold of the relative leaf age (a_{rel}) when the relative leaf efficiency (e_{rel}) starts to drop down from the maximum value ($e_{\text{rel}} = 1$), a_{bottom} is the threshold of a_{rel} when e_{rel} reaches the stable value after the drop down; a_{crit} is the leaf longevity or leaf critical age.

Given the parameters of our leaf-efficiency function (Figure 2 red dashed line, $a_{\text{drop}} = 0.2$, $a_{\text{bottom}} = 0.5$) as a suitable choice with leaf longevity equal to 2 yrs ($a_{\text{crit}} = 730$ days, that is 24 months) to represent the forests in our study area, following Equations 4 and 5, the values of a_{drop} and a_{bottom} for other potential "group of species" with different a_{crit} can be calculated by using Equation 6.

$$\alpha = \log_{a_{\text{crit}}}[a_{\text{drop}} + (a_{\text{bottom}} - a_{\text{drop}}) \times 0.5 + (1 - a_{\text{bottom}}) * 0.1] \tag{6}$$

Following Equation 6, Figure 10 shows how a_{crit}, a_{drop} and a_{bottom} ought to be coordinated to explain the bimodal phenology within the framework of the leaf economic spectrum. A larger difference between a_{drop} and a_{bottom} is observed with shorter leaf longevity (a_{crit}), interpreted by the increased slope of curves (Figures 11b and 11c). This implies that "species" with shorter leaf longevity usually should have higher A_{integral} and vice versa (Equation 4). Further tests with different a_{crit} (18, 12 and 6 months) but fixed a_{drop} (0.2) and a_{bottom} (0.5) show that, except for the simulation with $a_{\text{crit}} = 6$ months which cannot reproduce the two-peak seasonal variation of GPP, all simulations have good performances in reproducing the two peaks of the GPP seasonality (Figure S15 in Supporting Information S1). However, the modeled GPPs with these simulations have smaller amplitudes (1.38 and 1.31 gC m^2 day^{-1} for 18 and 12 months, respectively) and larger magnitudes (mean GPP are 8.49 and 8.42 gC m^2 day^{-1} for 18 and 12 months, respectively) (Tables S4 in Supporting Information S1). Although there is a lack of field observations of age-dependent leaf efficiency in central tropical African rainforests, our theoretical analysis suggests that the faster decrease of leaf efficiency is a potential photosynthetic investment strategy in central African rainforests, given its unique bimodal phenology. Furthermore, parameterization of a_{crit}, a_{drop} and a_{bottom} has a littile impact on the double-peak seasonality of modeled GPP (Figure 10 and Figure S15 in Supporting Information S1). This implies that, from the perspective of improving model performance, another potential solution is to regulate the fraction of each leaf age cohort by adjusting leaf ontogeny, thus affecting the

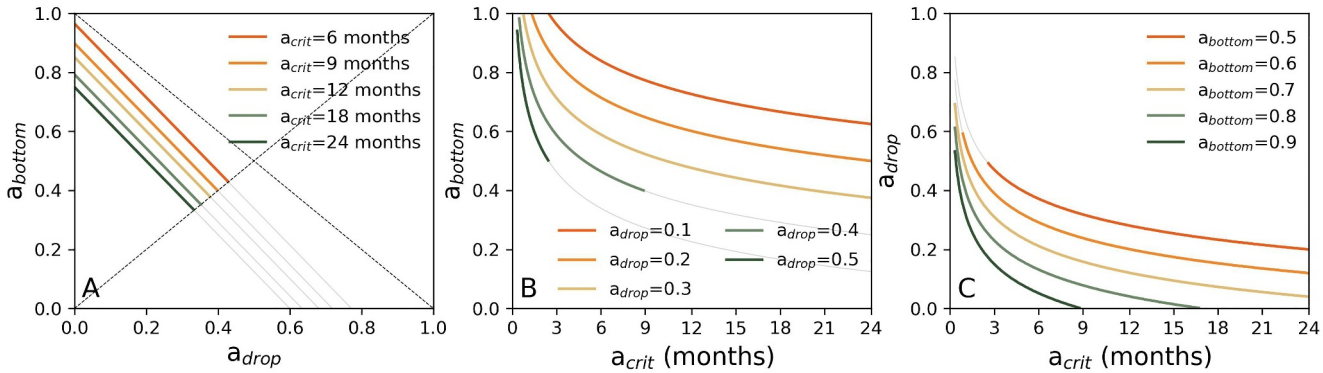

Figure 11. Illustration of the trade-off between leaf longevity (a_{crit}) and the integral of relative leaf efficiency ($A_{integral}$) which can be expressed as a function of a_{drop}, and a_{bottom} when assuming Equation 4a Relationship between a_{drop} and a_{bottom} with different a_{crit}, (b) Relationship between a_{crit} and a_{bottom} with different a_{drop}, (c) Relationship between a_{crit} and a_{drop} with different a_{bottom}. Colored solid curves indicate $a_{bottom} \geq a_{drop}$, while gray solid curves indicate invalid values where $a_{bottom} < a_{drop}$.

amplitude and magnitude of GPP. For example, introducing the climate-related parameter that increases the turnover of younger leaves while delaying the shedding of older leaves during the dry season could produce an older canopy with lower photosynthetic capacity.

The AFP model has poorer performances in the forests north of the equator (Figures 5 and 9) and exhibits improved performance as the synchronous between PRE and SWd increased. The distinct climate-phenology regimes in tropical African rainforests, identified by Yang et al. (2021), can explain this limitation. For the tropical forests situated in regions where PRE and SWd are synchronous, which mainly exit in Southeast Asia and tropical Africa (Wu et al., 2021; Yang et al., 2021), forests appear to prioritize light acquisition to maximize photosynthesis. In that case, old leaves are shed while new and more efficient leaves are produced as PRE and SWd increase in the early wet seasons (Descheemaeker et al., 2006). Conversely, in regions where PRE is asynchronous with SWd, forests experience a dry sunny season. Water stress resulting from soil water deficit and high VPD in the dry season can promote leaf abscission to reduce maintenance respiration costs, and insufficient rainfall predominantly constrains productivity until the wet season returns (Rowland et al., 2015; Xu et al., 2016). The AFP model overestimates LAI_{Young} (Figure 5) and GPP (Figure 6) from January to February when radiation is strong, especially in the NE and NW regions, where PRE and SWd are asynchronous during the first half of the year (Figure 7). This overestimation is also exhibited in another simulation that uses the VPD-triggered leaf-shedding scheme proposed by Chen et al. (2021) (Figure S11 in Supporting Information S1). During the period from January to February, high SWd or high VPD promote leaf shedding, while SWd-triggered leaf flushing scheme would produce more new leaves at the same time (Equation 1). However, simultaneously, insufficient rainfall would constraint productivity that inhibits the new leaf construction, which has been underestimated in the model. Therefore, our modeling framework has limited performance in modeling the phenology of tropical African forests where rainfall and radiation are asynchronous. In the future, adopting a more sophisticated phenology scheme considering the compound impacts of both water constrain and radiation on leaf phenology, such as the constraints of VPD on new leaf flushing, in the central tropical African rainforests could further improve the model performance. In addition, we suggest defining the vegetation map of African forests in the model by combining floristic information (Réjou-Méchain et al., 2021) and climate synchronicity regimes. Such a new PFT map would have different phenological parameterizations consistent with traits and climate.

Central tropical rainforests in Africa show very different behavior from the Amazon. There is a large-scale area with a unique bimodal phenology and photosynthesis, which is not observed in the Amazon. We argue that it is mainly because of different climate seasonality patterns. Central Africa has two wet- and dry-seasons and this unique climate seasonality pattern has given rise to this particular leaf phenology and photosynthesis of rainforests. It is more important that the coherence between SWd and PRE is opposite between central Africa and Amazon. The Amazon is dominated by asynchronous dynamics between SWd and PRE (Yang et al., 2021). And the drivers of photosynthesis show the transition from predominantly water-adapted in the southwest to light-adapted in the northeast (Liu et al., 2021; Xu et al., 2015). In central tropical African rainforests, however,

PRE and SWd mainly show synchronous dynamics (Figure 1a). Although the previous study with an SWd-triggered leaf phenology scheme (Chen et al., 2021) showed improvements over Amazon rainforests, it is necessary to develop a specific parameterization of this model for central tropical African rainforests, given the above differences between tropical Africa and Amazon in both climate and photosynthesis patterns. Our results also highlight that we need to split the presently unique ORCHIDEE PFT representing all tropical evergreen forests, into at least two to separately characterize the phenologies of tropical African rainforests and tropical Amazonian rainforests.

5. Conclusions

The central tropical African evergreen broadleaved forests exhibit a bimodal phenology, whose underlying mechanisms are poorly understood. This study using the ORCHIDEE LSM with new leaf shedding and leaf flushing schemes, both triggered by solar radiation (SWd), and a new leaf-age-dependent leaf efficiency strategy with four stages, has successfully modeled a two-peak seasonality of both LAI and GPP across central tropical African rainforests at both site and regional scales. The analysis of leaf ontogeny based on the leaf economics spectrum explores potential photosynthetic investment strategies in tropical African forests under the phenological scheme presented in this paper. This work is an important step toward the simulation of more realistic impacts of climate change over the tropics. Although in situ observations, satellite and model-based data sets have been used in this study, our ability to robustly evaluate the new phenology scheme is limited by the scarcity of in situ measurements, uncertainties in the remote-sensed and statistical data sets, as well as a lack of ecological knowledge about the processes that underpin this bimodal phenology of central tropical African forests. In the future, more in situ observed leaf phenology and photosynthesis data will be needed to bring potential improvements to the model. Further, we recommend extending current models, both AP for Amazon and APF for Africa in this work, to tropical evergreen forests in Southeast Asia to improve the photosynthesis and possibly transpiration modeling across the pan-tropics.

Data Availability Statement

All data used in this study are publicly available. The CRUJRA forcing data (Harris, 2019) is available at the website: https://catalogue.ceda.ac.uk/uuid/7f785c0e80aa4df2b39d068ce7351bbb. The MODIS Enhanced Vegetation Index (EVI) data (Didan, 2015) is available at the website: https://lpdaac.usgs.gov/products/mod13c2v006. The FLUXCOM GPP ($GPP_{FLUXCOM}$) data (Jung, 2021) is available at the website: https://www.fluxcom.org/CF-Download/. The FLUXNET GPP ($GPP_{FLUXSAT}$) data (Joiner & Yoshida, 2021) is available at the website: https://daac.ornl.gov/cgi-bin/dsviewer.pl?ds_id=1835. The BESS GPP (GPP_{BESS}) data (Jiang & Ryu, 2016b) is available at the website: https://www.environment.snu.ac.kr/bess-flux. The GOME-2 Solar-Induced Chlorophyll Fluorescence (SIF_{GOME-2}) data (Joiner et al., 2023) is available at the website: https://daac.ornl.gov/cgi-bin/dsviewer.pl?ds_id=2083. The CSIF data (Zhang, 2022) is available at the website: https://osf.io/8xqy6/. The model outputs and field data (Liu et al., 2024) used in this study are available at: https://doi.org/10.5281/zenodo.10683987. The ORCHIDEE-AFP model (Liu, 2024) code used in this study is open-source and distributed under the CeCILL (CEA CNRS INRIA Logiciel Libre) license. It is deposited at https://forge.ipsl.jussieu.fr/orchidee/wiki/GroupActivities/CodeAvalaibilityPublication/ORCHIDEE-AFP.

Acknowledgments

We would like to thank the editor and reviewers for their valuable time during the review of the paper. This study was supported by the National Natural Science Foundation of China (Grant 31971458, 41971275), Innovation Group Project of Southern Marine Science and Engineering Guangdong Laboratory (Zhuhai) (No 311021009), Belgian Science Policy Office (Belspo) Research Program for Earth Observation, STEREO III, Contract SR/00/334 (ECOPROPHET project), the Special high-level plan project of Guangdong Province (Grant 2016TQ03Z354), IDRC Grant "Climate change and increasing human-wildlife conflict", and the China Scholarship Council (CSC No 201904910317).

References

Abernethy, K., Bush, E. R., Forget, P. M., Mendoza, I., & Morellato, L. P. C. (2018). Current issues in tropical phenology: A synthesis. In *Biotropica*, (Vol. 50(3), pp. 477–482). https://doi.org/10.1111/btp.12558

Adamescu, G. S., Plumptre, A. J., Abernethy, K. A., Polansky, L., Bush, E. R., Chapman, C. A., et al. (2018). Annual cycles are the most common reproductive strategy in African tropical tree communities. *Biotropica*, *50*(3), 418–430. https://doi.org/10.1111/btp.12561

Adole, T., Dash, J., & Atkinson, P. M. (2016). A systematic review of vegetation phenology in Africa. In *Ecological informatics*, (Vol. 34, pp. 117–128). Elsevier B.V. https://doi.org/10.1016/j.ecoinf.2016.05.004

Babweteera, F., Plumptre, A. J., Adamescu, G. S., Shoo, L. P., Beale, C. M., Reynolds, V., et al. (2018). The ecology of tree reproduction in an African medium altitude rain forest. *Biotropica*, *50*(3), 405–417. https://doi.org/10.1111/btp.12563

Badgley, G., Field, C. B., & Berry, J. A. (2017). Canopy near-infrared reflectance and terrestrial photosynthesis. *Science Advances*, *3*(3), e1602244. https://doi.org/10.1126/SCIADV.1602244

Bontemps, S., Defourny, P., Radoux, J., van Bogaert, E., Lamarche, C., Achard, F., et al. (2013). Consistent global land cover maps for climate modelling communities: Current achievements of the ESA' land cover CCI. *ESASP*, *722*, 62. https://ui.adsabs.harvard.edu/abs/2013ESASP.722E.62B

Boucher, O., Servonnat, J., Albright, A. L., Aumont, O., Balkanski, Y., Bastrikov, V., et al. (2020). Presentation and evaluation of the IPSL-CM6A-LR climate model. *Journal of Advances in Modeling Earth Systems*, *12*(7), e2019MS002010. https://doi.org/10.1029/2019MS002010

Bradley, A. v., Gerard, F. F., Barbier, N., Weedon, G. P., Anderson, L. O., Huntingford, C., et al. (2011). Relationships between phenology, radiation and precipitation in the Amazon region. *Global Change Biology*, *17*(6), 2245–2260. https://doi.org/10.1111/J.1365-2486.2011.02405.X

Caen, A., Smallman, T. L., de Castro, A. A., Robertson, E., von Randow, C., Cardoso, M., & Williams, M. (2022). Evaluating two land surface models for Brazil using a full carbon cycle benchmark with uncertainties. *Climate Resilience and Sustainability*, *1*(1), e10. https://doi.org/10.1002/CLI2.10

Chapman, C. A., Valenta, K., Bonnell, T. R., Brown, K. A., & Chapman, L. J. (2018). Solar radiation and ENSO predict fruiting phenology patterns in a 15-year record from Kibale National Park, Uganda. *Biotropica*, *50*(3), 384–395. https://doi.org/10.1111/btp.12559

Chen, X., Ciais, P., Maignan, F., Zhang, Y., Bastos, A., Liu, L., et al. (2021). Vapor pressure deficit and sunlight explain seasonality of leaf phenology and photosynthesis across Amazonian evergreen broadleaved forest. *Global Biogeochemical Cycles*, *35*(6), e2020GB006893. https://doi.org/10.1029/2020GB006893

Chen, X., Maignan, F., Viovy, N., Bastos, A., Goll, D., Wu, J., et al. (2020). Novel representation of leaf phenology improves simulation of Amazonian evergreen forest photosynthesis in a land surface model. *Journal of Advances in Modeling Earth Systems*, *12*(1), e2018MS001565. https://doi.org/10.1029/2018MS001565

Coley, P. D., & Barone, J. A. (1996). Herbivory and plant defenses in tropical forests. *Annual Review of Ecology and Systematics*, *27*(1), 305–335. https://doi.org/10.1146/annurev.ecolsys.27.1.305

Cooper, D. L. M., Lewis, S. L., Sullivan, M. J. P., Prado, P. I., ter Steege, H., Barbier, N., et al. (2024). Consistent patterns of common species across tropical tree communities. *Nature*, *625*(7996), 1–10. https://doi.org/10.1038/s41586-023-06820-z

Couralet, C., Van den Bulcke, J., Ngoma, L. M., Van Acker, J., & Beeckman, H. (2013). Phenology in functional groups of central African rainforest trees. *Journal of Tropical Forest Science*, 361–374.

Cucchi, M., Weedon, G. P., Amici, A., Bellouin, N., Lange, S., Müller Schmied, H., et al. (2020). WFDE5: Bias-adjusted ERA5 reanalysis data for impact studies. *Earth System Science Data*, *12*(3), 2097–2120. https://doi.org/10.5194/essd-12-2097-2020

Descheemaeker, K., Muys, B., Nyssen, J., Poesen, J., Raes, D., Haile, M., & Deckers, J. (2006). Litter production and organic matter accumulation in exclosures of the Tigray highlands, Ethiopia. *Forest Ecology and Management*, *233*(1), 21–35. https://doi.org/10.1016/j.foreco.2006.05.061

De Weirdt, M., Verbeeck, H., Maignan, F., Peylin, P., Poulter, B., Bonal, D., et al. (2012). Seasonal leaf dynamics for tropical evergreen forests in a process-based global ecosystem model. *Geoscientific Model Development*, *5*(5), 1091–1108. https://doi.org/10.5194/gmd-5-1091-2012

Didan, K. (2015). MOD13C2 MODIS/Terra vegetation indices monthly L3 global 0.05Deg CMG [Dataset]. *NASA LP DAAC*. https://doi.org/10.5067/MODIS/MOD13C2.006

Dommo, A., Philippon, N., Vondou, D. A., Sèze, G., & Eastman, R. (2018). The June–September low cloud cover in Western central Africa: Mean spatial distribution and diurnal evolution, and associated atmospheric dynamics. *Journal of Climate*, *31*(23), 9585–9603. https://doi.org/10.1175/JCLI-D-17-0082.1

Feldman, A. F., Short Gianotti, D. J., Konings, A. G., McColl, K. A., Akbar, R., Salvucci, G. D., & Entekhabi, D. (2018). Moisture pulse-reserve in the soil-plant continuum observed across biomes. *Nature Plants*, *4*(12), 1026–1033. https://doi.org/10.1038/s41477-018-0304-9

Feldman, A. F., Short Gianotti, D. J., Trigo, I. F., Salvucci, G. D., & Entekhabi, D. (2019). Satellite-based assessment of land surface energy partitioning–soil moisture relationships and effects of confounding variables. *Water Resources Research*, *55*(12), 10657–10677. https://doi.org/10.1029/2019WR025874

Fu, R., Yin, L., Li, W., Arias, P. A., Dickinson, R. E., Huang, L., et al. (2013). Increased dry-season length over southern Amazonia in recent decades and its implication for future climate projection. *Proceedings of the National Academy of Sciences of the United States of America*, *110*(45), 18110–18115. https://doi.org/10.1073/PNAS.1302584110

Galvão, L. S., dos Santos, J. R., Roberts, D. A., Breunig, F. M., Toomey, M., & de Moura, Y. M. (2011). On intra-annual EVI variability in the dry season of tropical forest: A case study with MODIS and hyperspectral data. *Remote Sensing of Environment*, *115*(9), 2350–2359. https://doi.org/10.1016/J.RSE.2011.04.035

Gonçalves, N. B., Lopes, A. P., Dalagnol, R., Wu, J., Pinho, D. M., & Nelson, B. W. (2020). Both near-surface and satellite remote sensing confirm drought legacy effect on tropical forest leaf phenology after 2015/2016 ENSO drought. *Remote Sensing of Environment*, *237*, 111489. https://doi.org/10.1016/J.RSE.2019.111489

Gond, V., Fayolle, A., Pennec, A., Cornu, G., Mayaux, P., Camberlin, P., et al. (2013). Vegetation structure and greenness in Central Africa from Modis multi-temporal data. *Philosophical Transactions of the Royal Society B: Biological Sciences*, *368*(1625), 20120309. https://doi.org/10.1098/RSTB.2012.0309

Gong, F., Chen, X., Yuan, W., Su, Y., Yang, X., Liu, L., et al. (2022). Partitioning of three phenology rhythms in American tropical and subtropical forests using remotely sensed solar-induced chlorophyll fluorescence and field litterfall observations. *International Journal of Applied Earth Observation and Geoinformation*, *107*, 102698. https://doi.org/10.1016/j.jag.2022.102698

Graham, E. A., Mulkey, S. S., Kitajima, K., Phillips, N. G., & Wright, S. J. (2003). Cloud cover limits net CO_2 uptake and growth of a rainforest tree during tropical rainy seasons. *Proceedings of the National Academy of Sciences*, *100*(2), 572–576. https://doi.org/10.1073/PNAS.0133045100

Green, J. K., Berry, J., Ciais, P., Zhang, Y., & Gentine, P. (2020). Amazon rainforest photosynthesis increases in response to atmospheric dryness. *Science Advances*, *6*(47), eabb7232. https://doi.org/10.1126/sciadv.abb7232

Guan, K., Wolf, A., Medvigy, D., Caylor, K. K., Pan, M., Wood, E. F., et al. (2013). Seasonal coupling of canopy structure and function in African tropical forests and its environmental controls. *Ecosphere*, *4*(3), 1–21. https://doi.org/10.1890/ES12-00232.1

Harris, I., Jones, P. D., Osborn, T. J., & Lister, D. H. (2014). Updated high-resolution grids of monthly climatic observations – The CRU TS3.10 dataset. *International Journal of Climatology*, *34*(3), 623–642. https://doi.org/10.1002/JOC.3711

Harris, I. C. (2019). CRU JRA v2.0: A forcings dataset of gridded land surface blend of Climatic Research Unit (CRU) and Japanese Reanalysis (JRA) data; Jan.1901—Dec.2018 [Dataset]. *Centre for Environmental Data Analysis CEDA Archive*. https://catalogue.ceda.ac.uk/uuid/7f785c0e80aa4df2b39d068ce7351bbb

He, L., Chen, J. M., Liu, J., Mo, G., & Joiner, J. (2017). Angular normalization of GOME-2 Sun-induced chlorophyll fluorescence observation as a better proxy of vegetation productivity. *Geophysical Research Letters*, *44*(11), 5691–5699. https://doi.org/10.1002/2017GL073708

Huete, A., Didan, K., Miura, T., Rodriguez, E. P., Gao, X., & Ferreira, L. G. (2002). Overview of the radiometric and biophysical performance of the MODIS vegetation indices. *Remote Sensing of Environment*, *83*(1–2), 195–213. https://doi.org/10.1016/S0034-4257(02)00096-2

Ishida, A., Toma, T., & Marjenah (1999). Limitation of leaf carbon gain by stomatal and photochemical processes in the top canopy of Macaranga Conifera, a tropical pioneer tree. *Tree Physiology*, *19*(7), 467–473. https://doi.org/10.1093/TREEPHYS/19.7.467

Jiang, C., & Ryu, Y. (2016a). Multi-scale evaluation of global gross primary productivity and evapotranspiration products derived from Breathing Earth System Simulator (BESS). *Remote Sensing of Environment*, *186*, 528–547. https://doi.org/10.1016/j.rse.2016.08.030

Jiang, C., & Ryu, Y. (2016b). Global gross primary productivity and evapotranspiration products derived from Breathing Earth System Simulator (BESS). [Dataset]. *Ecological Sensing AI Lab, SNU*. https://www.environment.snu.ac.kr/bess-flux

Jiang, Y., Zhou, L., Tucker, C. J., Raghavendra, A., Hua, W., Liu, Y. Y., & Joiner, J. (2019). Widespread increase of boreal summer dry season length over the Congo rainforest. In *Nature climate change*, (Vol. 9(8), pp. 617–622). Nature Publishing Group. https://doi.org/10.1038/s41558-019-0512-y

Joiner, J., Guanter, L., Lindstrot, R., Voigt, M., Vasilkov, A. P., Middleton, E. M., et al. (2013). Global monitoring of terrestrial chlorophyll fluorescence from moderate-spectral-resolution near-infrared satellite measurements: Methodology, simulations, and application to GOME-2. *Atmospheric Measurement Techniques*, *6*(10), 2803–2823. https://doi.org/10.5194/AMT-6-2803-2013

Joiner, J., & Yoshida, Y. (2021). *Global MODIS and FLUXNET-derived daily gross primary production, V2*. ORNL DAAC. https://doi.org/10.3334/ORNLDAAC/1835

Joiner, J., Yoshida, Y., Guanter, L., & Middleton, E. M. (2016). New methods for the retrieval of chlorophyll red fluorescence from hyperspectral satellite instruments: Simulations and application to GOME-2 and SCIAMACHY. *Atmospheric Measurement Techniques*, *9*(8), 3939–3967. https://doi.org/10.5194/AMT-9-3939-2016

Joiner, J., Yoshida, Y., Koehler, P., Frankenberg, C., & Parazoo, N. C. (2023). L2 daily Solar-Induced Fluorescence (SIF) from MetOp-A GOME-2, 2007-2018 [Dataset]. *ORNL DAAC*. https://doi.org/10.3334/ORNLDAAC/2083

Joiner, J., Yoshida, Y., Zhang, Y., Duveiller, G., Jung, M., Lyapustin, A., et al. (2018). Remote sensing estimation of terrestrial global Gross Primary Production (GPP) with Satellite data-driven models and eddy covariance flux data. https://doi.org/10.3390/rs10080000

Jung, M. (2021). FluxCom carbon fluxes. [Dataset]. *FluxCom*. https://www.fluxcom.org/CF-Download/

Jung, M., Schwalm, C., Migliavacca, M., Walther, S., Camps-Valls, G., Koirala, S., et al. (2020). Scaling carbon fluxes from eddy covariance sites to globe: Synthesis and evaluation of the FLUXCOM approach. *Biogeosciences*, *17*(5), 1343–1365. https://doi.org/10.5194/bg-17-1343-2020

Kattge, J., & Knorr, W. (2007). Temperature acclimation in a biochemical model of photosynthesis: A reanalysis of data from 36 species. *Plant, Cell and Environment*, *30*(9), 1176–1190. https://doi.org/10.1111/j.1365-3040.2007.01690.x

Kearsley, E., de Haulleville, T., Hufkens, K., Kidimbu, A., Toirambe, B., Baert, G., et al. (2013). Conventional tree height-diameter relationships significantly overestimate aboveground carbon stocks in the Central Congo Basin. *Nature Communications*, *4*(1), 2269. https://doi.org/10.1038/ncomms3269

Kearsley, E., Verbeeck, H., Stoffelen, P., Janssens, S. B., Yakusu, E. K., Kosmala, M., et al. (2024). Historical tree phenology data reveal the seasonal rhythms of the Congo Basin rainforest. *Plant-Environment Interactions*, *5*(2), e10136. https://doi.org/10.1002/pei3.10136

Kobayashi, S., Ota, Y., Harada, Y., Ebita, A., Moriya, M., Onoda, H., et al. (2015). The JRA-55 reanalysis: General specifications and basic characteristics. *Journal of the Meteorological Society of Japan. Ser. II*, *93*(1), 5–48. https://doi.org/10.2151/JMSJ.2015-001

Koven, C. D., Ringeval, B., Friedlingstein, P., Ciais, P., Cadule, P., Khvorostyanov, D., et al. (2011). Permafrost carbon-climate feedbacks accelerate global warming. *Proceedings of the National Academy of Sciences of the United States of America*, *108*(36), 14769–14774. https://doi.org/10.1073/PNAS.1103910108

Krinner, G., Viovy, N., de Noblet-Ducoudré, N., Ogée, J., Polcher, J., Friedlingstein, P., et al. (2005). A dynamic global vegetation model for studies of the coupled atmosphere-biosphere system. In *Global biogeochemical cycles*, Vol. 19(1), pp. 1–33. https://doi.org/10.1029/2003GB002199

Leff, J. W., Wieder, W. R., Taylor, P. G., Townsend, A. R., Nemergut, D. R., Grandy, A. S., & Cleveland, C. C. (2012). Experimental litterfall manipulation drives large and rapid changes in soil carbon cycling in a wet tropical forest. *Global Change Biology*, *18*(9), 2969–2979. https://doi.org/10.1111/J.1365-2486.2012.02749.X

Lewis, S. L., Lopez-Gonzalez, G., Sonké, B., Affum-Baffoe, K., Baker, T. R., Ojo, L. O., et al. (2009). Increasing carbon storage in intact African tropical forests. *Nature*, *457*(7232), 1003–1006. https://doi.org/10.1038/nature07771

Li, Q., Chen, X., Yuan, W., Lu, H., Shen, R., Wu, S., et al. (2021). Remote sensing of seasonal climatic constraints on leaf phenology across pantropical evergreen forest biome. *Earth's Future*, *9*(9), e2021EF002160. https://doi.org/10.1029/2021EF002160

Liu, L. (2024). ORCHIDEE-AFP [Software]. *ORCHIDEE-Wiki*. https://forge.ipsl.jussieu.fr/orchidee/wiki/GroupActivities/CodeAvalaibilityPublication/ORCHIDEE-AFP

Liu, L., Ciais, P., Maignan, F., Zhang, Y., Viovy, N., Peaucelle, M., et al. (2024). Solar radiation triggers the bimodal leaf phenology of central African evergreen broadleaved forests [Dataset]. *Zenodo*. https://doi.org/10.5281/zenodo.10683987

Liu, L., Gong, F., Chen, X., Su, Y., Fan, L., Wu, S., et al. (2022). Bidirectional drought-related canopy dynamics across pantropical forests: A satellite-based statistical analysis. *Remote Sensing in Ecology and Conservation*, *8*(1), 72–91. https://doi.org/10.1002/rse2.229

Liu, L., Yang, X., Gong, F., Su, Y., Huang, G., & Chen, X. (2021). The Novel Microwave Temperature Vegetation Drought Index (MTVDI) captures canopy seasonality across Amazonian tropical evergreen forests. *Remote Sensing 2021*, *13*(3), 339. https://doi.org/10.3390/RS13030339

Malhi, Y., Adu-Bredu, S., Asare, R. A., Lewis, S. L., & Mayaux, P. (2013). The past, present and future of Africa's rainforests. *Philosophical Transactions of the Royal Society B: Biological Sciences*, *368*(1625), 20120293. https://doi.org/10.1098/RSTB.2012.0293

Manoli, G., Ivanov, V. Y., & Fatichi, S. (2018). Dry-season greening and water stress in Amazonia: The role of modeling leaf phenology. *Journal of Geophysical Research: Biogeosciences*, *123*(6), 1909–1926. https://doi.org/10.1029/2017JG004282

Martens, B., Miralles, D. G., Lievens, H., Van Der Schalie, R., De Jeu, R. A. M., Fernández-Prieto, D., et al. (2017). GLEAM v3: Satellite-based land evaporation and root-zone soil moisture. *Geoscientific Model Development*, *10*(5), 1903–1925. https://doi.org/10.5194/gmd-10-1903-2017

Menezes, J., Garcia, S., Grandis, A., Nascimento, H., Domingues, T. F., Guedes, A. v., et al. (2022). Changes in leaf functional traits with leaf age: When do leaves decrease their photosynthetic capacity in Amazonian trees? *Tree Physiology*, *42*(5), 922–938. https://doi.org/10.1093/treephys/tpab042

Miralles, D. G., Holmes, T. R. H., De Jeu, R. A. M., Gash, J. H., Meesters, A. G. C. A., & Dolman, A. J. (2011). Global land-surface evaporation estimated from satellite-based observations. *Hydrology and Earth System Sciences*, *15*(2), 453–469. https://doi.org/10.5194/hess-15-453-2011

Misson, L., Tu, K., Boniello, R. A., & Goldstein, A. H. (2006). Seasonality of photosynthetic parameters in a multi-specific and vertically complex forest ecosystem in the Sierra Nevada of California. *Tree Physiology*, *26*(6), 729–741. https://doi.org/10.1093/TREEPHYS/26.6.729

Nicholson, S. E. (2018). The ITCZ and the seasonal cycle over equatorial Africa. *Bulletin of the American Meteorological Society*, *99*(2), 337–348. https://doi.org/10.1175/BAMS-D-16-0287.1

Niinemets, Ü., Sun, Z., & Talts, E. (2015). Controls of the quantum yield and saturation light of isoprene emission in different-aged aspen leaves. *Plant, Cell and Environment*, *38*(12), 2707–2720. https://doi.org/10.1111/PCE.12582

Osnas, J. L. D., Lichstein, J. W., Reich, P. B., & Pacala, S. W. (2013). Global leaf trait relationships: Mass, area, and the leaf economics spectrum. *Science*, *340*(6133), 741–744. https://doi.org/10.1126/SCIENCE.1231574

Peñuelas, J., Rutishauser, T., & Filella, I. (2009). Phenology feedbacks on climate change. *Science*, *324*(5929), 887–888. https://doi.org/10.1126/SCIENCE.1173004

Philippon, N., Cornu, G., Monteil, L., Gond, V., Moron, V., Pergaud, J., et al. (2019). The light-deficient climates of Western Central African evergreen forests. *Environmental Research Letters*, *14*(3), 034007. https://doi.org/10.1088/1748-9326/aaf5d8

Philippon, N., de Lapparent, B., Gond, V., Sèze, G., Martiny, N., Camberlin, P., et al. (2016). Analysis of the diurnal cycles for a better understanding of the mean annual cycle of forests greenness in Central Africa. *Agricultural and Forest Meteorology*, *223*, 81–94. https://doi.org/10.1016/J.AGRFORMET.2016.04.005

Prentice, I. C., Cramer, W., Harrison, S. P., Leemans, R., Monserud, R. A., & Solomon, A. M. (1992). A global biome model based on plant physiology and dominance, soil properties and climate. *Journal of Biogeography*, *19*(2), 117. https://doi.org/10.2307/2845499

Raghavendra, A., Zhou, L., Jiang, Y., & Hua, W. (2018). Increasing extent and intensity of thunderstorms observed over the Congo Basin from 1982 to 2016. *Atmospheric Research*, *213*, 17–26. https://doi.org/10.1016/J.ATMOSRES.2018.05.028

Réjou-Méchain, M., Mortier, F., Bastin, J.-F., Cornu, G., Barbier, N., Bayol, N., et al. (2021). Unveiling African rainforest composition and vulnerability to global change. *Nature*, *593*(7857), 90–94. https://doi.org/10.1038/s41586-021-03483-6

Rowland, L., da Costa, A. C. L., Galbraith, D. R., Oliveira, R. S., Binks, O. J., Oliveira, A. a. R., et al. (2015). Death from drought in tropical forests is triggered by hydraulics not carbon starvation. *Nature*, *528*(7580), 119–122. https://doi.org/10.1038/nature15539

Ryu, Y., Baldocchi, D. D., Kobayashi, H., van Ingen, C., Li, J., Black, T. A., et al. (2011). Integration of MODIS land and atmosphere products with a coupled-process model to estimate gross primary productivity and evapotranspiration from 1 km to global scales. *Global Biogeochemical Cycles*, *25*(4). https://doi.org/10.1029/2011GB004053

Santiago, L. S., & Wright, S. J. (2007). Leaf functional traits of tropical forest plants in relation to growth form. *Functional Ecology*, *21*(1), 19–27. https://doi.org/10.1111/j.1365-2435.2006.01218.x

Sayer, E. J., Heard, M. S., Grant, H. K., Marthews, T. R., & Tanner, E. V. J. (2011). Soil carbon release enhanced by increased tropical forest litterfall. *Nature Climate Change*, *1*(6), 304–307. https://doi.org/10.1038/nclimate1190

Shipley, B., Lechowicz, M. J., Wright, I., & Reich, P. B. (2006). Fundamental trade-offs generating the worldwide leaf economics spectrum. *Ecology*, *87*(3), 535–541. https://doi.org/10.1890/05-1051

Sitch, S., Smith, B., Prentice, I. C., Arneth, A., Bondeau, A., Cramer, W., et al. (2003). Evaluation of ecosystem dynamics, plant geography and terrestrial carbon cycling in the LPJ dynamic global vegetation model. *Global Change Biology*, *9*(2), 161–185. https://doi.org/10.1046/J.1365-2486.2003.00569.X

Sorí, R., Nieto, R., Vicente-Serrano, S. M., Drumond, A., & Gimeno, L. (2017). A Lagrangian perspective of the hydrological cycle in the Congo River basin. *Earth System Dynamics*, *8*(3), 653–675. https://doi.org/10.5194/ESD-8-653-2017

Sun, Y., Knyazikhin, Y., She, X., Ni, X., Chen, C., Ren, H., & Myneni, R. B. (2022). Seasonal and long-term variations in leaf area of Congolese rainforest. *Remote Sensing of Environment*, *268*, 112762. https://doi.org/10.1016/j.rse.2021.112762

Tang, H., & Dubayah, R. (2017). Light-driven growth in Amazon evergreen forests explained by seasonal variations of vertical canopy structure. *Proceedings of the National Academy of Sciences*, *114*(10), 2640–2644. https://doi.org/10.1073/pnas.1616943114

Tramontana, G., Jung, M., Schwalm, C. R., Ichii, K., Camps-Valls, G., Ráduly, B., et al. (2016). Predicting carbon dioxide and energy fluxes across global FLUXNET sites with regression algorithms. *Biogeosciences*, *13*(14), 4291–4313. https://doi.org/10.5194/BG-13-4291-2016

Vallicrosa, H., Sardans, J., Maspons, J., Zuccarini, P., Fernández-Martínez, M., Bauters, M., et al. (2021). Global maps and factors driving forest foliar elemental composition: The importance of evolutionary history. *New Phytologist*, *233*(1), 169–181. https://doi.org/10.1111/NPH.17771

Verhegghen, A., Mayaux, P., de Wasseige, C., & Defourny, P. (2012). Mapping Congo Basin vegetation types from 300 m and 1 km multi-sensor time series for carbon stocks and forest areas estimation. *Biogeosciences*, *9*(12), 5061–5079. https://doi.org/10.5194/BG-9-5061-2012

Wilson, A. M., & Jetz, W. (2016). Remotely sensed high-resolution global cloud dynamics for predicting ecosystem and biodiversity distributions. *PLoS Biology*, *14*(3), e1002415. https://doi.org/10.1371/JOURNAL.PBIO.1002415

Winbourne, J. B., & McCulloch, L. A. (2022). Herbivores drive scarcity of some nitrogen-fixing tropical trees. *Nature*, *612*(7940), 411–412. https://doi.org/10.1038/d41586-022-04170-w

Wright, I. J., Reich, P. B., Westoby, M., Ackerly, D. D., Baruch, Z., Bongers, F., et al. (2004). The worldwide leaf economics spectrum. *Nature*, *428*(6985), 821–827. https://doi.org/10.1038/nature02403

Wright, J. S., Fu, R., Worden, J. R., Chakraborty, S., Clinton, N. E., Risi, C., et al. (2017). Rainforest-initiated wet season onset over the southern Amazon. *Proceedings of the National Academy of Sciences of the United States of America*, *114*(32), 8481–8486. https://doi.org/10.1073/PNAS.1621516114

Wu, J., Albert, L. P., Lopes, A. P., Restrepo-Coupe, N., Hayek, M., Wiedemann, K. T., et al. (2016). Leaf development and demography explain photosynthetic seasonality in Amazon evergreen forests. *Science*, *351*(6276), 972–976. https://doi.org/10.1126/science.aad5068

Wu, J., Su, Y., Chen, X., Liu, L., Yang, X., Gong, F., et al. (2021). Leaf shedding of Pan-Asian tropical evergreen forests depends on the synchrony of seasonal variations of rainfall and incoming solar radiation. *Agricultural and Forest Meteorology*, *311*, 108691. https://doi.org/10.1016/j.agrformet.2021.108691

Xu, L., Saatchi, S. S., Yang, Y., Myneni, R. B., Frankenberg, C., Chowdhury, D., & Bi, J. (2015). Satellite observation of tropical forest seasonality: Spatial patterns of carbon exchange in Amazonia. *Environmental Research Letters*, *10*(8), 084005. https://doi.org/10.1088/1748-9326/10/8/084005

Xu, X., Medvigy, D., Powers, J. S., Becknell, J. M., & Guan, K. (2016). Diversity in plant hydraulic traits explains seasonal and inter-annual variations of vegetation dynamics in seasonally dry tropical forests. *New Phytologist*, *212*(1), 80–95. https://doi.org/10.1111/nph.14009

Yan, D., Zhang, X., Yu, Y., & Guo, W. (2016). A comparison of tropical rainforest phenology Retrieved from geostationary (SEVIRI) and polar-orbiting (MODIS) sensors across the Congo basin. *IEEE Transactions on Geoscience and Remote Sensing*, *54*(8), 4867–4881. https://doi.org/10.1109/TGRS.2016.2552462

Yan, D., Zhang, X., Yu, Y., & Guo, W. (2017). Characterizing land cover impacts on the responses of land surface phenology to the rainy season in the Congo basin. *Remote Sensing*, *9*(5), 461. https://doi.org/10.3390/rs9050461

Yang, X., Wu, J., Chen, X., Ciais, P., Maignan, F., Yuan, W., et al. (2021). A comprehensive framework for seasonal controls of leaf abscission and productivity in evergreen broadleaved tropical and subtropical forests. *The Innovation*, *2*(4), 100154. https://doi.org/10.1016/j.xinn.2021.100154

Zeng, Y., Hao, D., Park, T., Zhu, P., Huete, A., Myneni, R., et al. (2023). Structural complexity biases vegetation greenness measures. *Nature Ecology & Evolution*, *7*(11), 1790–1798. https://doi.org/10.1038/s41559-023-02187-6

Zhang, Y. (2022). Contiguous Solar Induced chlorophyll Fluorescence (CSIF) [Dataset]. *OSFHOME*. https://osf.io/8xqy6/

Zhang, Y., Joiner, J., Hamed Alemohammad, S., Zhou, S., & Gentine, P. (2018). A global spatially Contiguous Solar-Induced Fluorescence (CSIF) dataset using neural networks. *Biogeosciences*, *15*(19), 5779–5800. https://doi.org/10.5194/BG-15-5779-2018

Zhang, Y., Zhu, Z., Liu, Z., Zeng, Z., Ciais, P., Huang, M., et al. (2016). Seasonal and interannual changes in vegetation activity of tropical forests in Southeast Asia. *Agricultural and Forest Meteorology*, *224*, 1–10. https://doi.org/10.1016/J.AGRFORMET.2016.04.009

Zhou, L., Tian, Y., Myneni, R. B., Ciais, P., Saatchi, S., Liu, Y. Y., et al. (2014). Widespread decline of Congo rainforest greenness in the past decade. *Nature*, *508*(7498), 86–90. https://doi.org/10.1038/nature13265

Zhou, X., Xin, Q., Dai, Y., & Li, W. (2021). A deep-learning-based experiment for benchmarking the performance of global terrestrial vegetation phenology models. *Global Ecology and Biogeography*, *30*(11), 2178–2199. https://doi.org/10.1111/GEB.13374

Zhu, Z., Bi, J., Pan, Y., Ganguly, S., Anav, A., Xu, L., et al. (2013). Global data sets of vegetation Leaf Area Index (LAI)3g and Fraction of Photosynthetically Active Radiation (FPAR)3g derived from Global Inventory Modeling and Mapping Studies (GIMMS) Normalized Difference Vegetation Index (NDVI3g) for the period 1981 to 2011. *Remote Sensing*, *5*(2), 927–948. https://doi.org/10.3390/RS5020927